NAM

Kinematic modelling of large tremors in the Groningen field using extended seismic sources
Huizinge Earthquake Part 1

H.M. Wentinck

Datum August 2017

Editors Jan van Elk, & Dirk Doornhof

General Introduction

The Huizinge earthquake of 16th August 2012 with a magnitude of M_L = 3.6 had a profound impact on the Groningen community and led to the acceleration of the research program into induced seismicity in Groningen. As part of this program new capabilities were developed. For instance, geomechanical modelling of rupture processes taking place in the depleted gas reservoir of the Rotliegend formation was improved.

Using these capabilities, this report revisits the Huizinge earthquake of 2012. Using kinematic modelling of the earthquake, an attempt is made to estimate the rupture dimensions of this earthquake based on the surface recordings.

NAM

Title	**Kinematic modelling of large tremors in the Groningen field using extended seismic sources Huizinge Earthquake Part 1**		**Date**	August 2017
			Initiator	NAM
Author(s)	H.M. Wentinck	**Editor**	Jan van Elk and Dirk Doornhof	
Organisation	Team of Academic Experts	**Organisation**	NAM	
Place in the Study and Data Acquisition Plan	Study Theme: Geomechanical Modelling Comment: The Huizinge earthquake of 16th August 2012 with a magnitude of M_L = 3.6 had a profound impact on the Groningen community and led to the acceleration of the research program into induced seismicity in Groningen. As part of this program new capabilities were developed. For instance, geomechanical modelling of rupture processes taking place in the depleted gas reservoir of the Rotliegend formation was improved. Using these capabilities, this report revisits the Huizinge earthquake of 2012. Using kinematic modelling of the earthquake, an attempt is made to estimate the rupture dimensions of this earthquake based on the surface recordings.			
Directly linked research	1. Reservoir engineering studies in the pressure depletion for different production scenarios. 2. Seismic monitoring activities; both the extension of the geophone network and the installation on geophones in deep wells. 3. Geomechanical studies 4. Subsidence and compaction studies.			
Used data	KNMI Earthquake catalogue Geological maps of faults in the Rotliegend reservoir			
Associated organisation	Shell Global Solutions			
Assurance				

report for NAM 2017

Kinematic modelling of large tremors in the Groningen field using extended seismic sources

first results related to the Huizinge 2012 tremor

by

H.M. Wentinck

Executive Summary

This work is about the kinematic modelling of the relatively large Huizinge tremor in the Groningen field, using an extended seismic source. In particular, we have explored the possibility to derive from the ground motions, as recorded by nearby ground accelerometers, the rupture plane dimensions.
The kinematic model includes reasonable proxys for the horizons between the geological formations in the overburden and for the primary and secondary wave velocities in these formations. The seismic source is represented by a series of double couple point forces along fault strike on the rupture plane.

We show a possible seismic source for the Huizinge tremor with reservations. Differences between the ground motions from an extended source and a point source with the same fault orientation and slip direction are subtle and with the present uncertainties about the orientation of the ground accelerometers in the horizontal plane not easily resolved.

The present results suggest that the double peak in the radial displacement component following from this tremor, as recorded by the Middelstum-1 and Kantens ground accelerometers, is not due to multiple scattering of the waves in the overburden. A suggestion, that it follows from two seismic events occurring quickly after each other, has to be confirmed or rejected by additional simulations.

Table of Contents

Table 0.1 : List of frequently used symbols

Symbol	Property	Unit
$\boldsymbol{a}$	displacement acceleration vector	m/s^2
D	relative displacement or slip over a slip plane	m
D	damping or isotropic loss factor for attenuation of seismic waves	-
f	frequency	s^{-1}
f_c	corner frequency of the ground motions	Hz
f_{stf}	source time function	-
f	magnitude of a point force	N
$\boldsymbol{f}$	force vector	N
$\boldsymbol{l}$	unit vector in the slip direction	-
i_ζ	take-off angle of body wave from source	degree/radian
k	wave number	m^{-1}
l_{DC}	arm of the double couple	m
L	length of rupture plane along fault strike	m
M	moment magnitude	Richter
M_L	local magnitude	Richter
$\boldsymbol{m}$	moment tensor defining the slip plane orientation and slip direction	-
$\boldsymbol{M}$	moment tensor	Nm
M_0	seismic moment	Nm
n	shape parameter of modified source time function	-
$\boldsymbol{n}$	unit vector normal to the slip plane	-
Q	quality factor for attenuation of seismic waves	m
s	distance between seismic source and receiver	m
s_h	distance between epicentre and receiver	m
S	surface area of rupture plane	m^2
t	time	s
t_{nucl}	time of nucleation of the rupture	s
t_{onset}	onset time of source time function	s
t_r	rise time of source time function	s
t_R	duration of the rupture in the slip plane	s
$t_{trigger}$	trigger time of a point force of an extended source	s
Δt_{ps}	time difference between the arrivals of primary and secondary waves	s
$\boldsymbol{u}$	displacement vector	m
V_p	velocity of primary wave	m/s
V_s	velocity of secondary wave	m/s
V_r	rupture velocity	m/s
$V_{r,strike}$	rupture velocity along fault strike	m/s
$\boldsymbol{v}$	displacement velocity vector	m/s
W	width of rupture plane along fault dip	m
$\boldsymbol{x}$	Cartesian coordinates of the receiver (or location in the field)	m
x, y, z	coordinates used for the analytical solutions	m
X, Y, Z	coordinates based on the Dutch Rijksdriehoeksstelsel	m

Table 0.2 : List of frequently used symbols, continued

Symbol	Property	Unit
α	primary wave velocity (V_p)	m/s
α_{dM}	Rayleigh damping factor	s^{-1}
β	secondary wave velocity (V_s)	m/s
β_{dM}	Rayleigh damping factor	s
δ	dip angle of fault	degree/radian
γ_i	direction cosinus of the receiver with respect to the source	-
δ_{ij}	Kronecker delta function	-
$\Delta\tau$	stress drop over fault plane during rupture	Pa
ζ	damping or isotropic loss factor for the attenuation of seismic waves	-
$\boldsymbol{\zeta}$	Cartesian coordinates of the source	m
λ	first Lamé parameter	Pa
λ	wavelength	m
λ	rake angle of slip vector	degree/radian
μ	shear modulus of rock or second Lamé parameter	Pa
ν	Poisson ratio	Pa
ρ	mass density of rock	kg/m^3
τ	time	s
ϕ	fault strike azimuth angle	degree/radian
ϕ'	receiver azimuth angle	degree/radian
ω	angular or circular frequency of a wave	radian/s

Table 0.3 : List of frequently used symbols, continued

Symbol	Refers to
.....	.....
superscripts	
*	complex number
subscripts	
area	selected region or area
arr	arrival time of wave at receiver
DC	double couple
hor	horizontal component of displacmement, velocity or acceleration
p	primary or compressive wave
rad	radial component of displacement, velocity or acceleration
rec	receiver or geophone
rms	root mean square value
s	secondary or shear wave
stf	source time function
strike	along fault strike
tra	transverse component of displacement, velocity or acceleration
ver	vertical component of displacement, velocity or acceleration
abbreviations	
DOF	Degrees of Freedom
DR	Dutch Rijksdriehoeksstelsel coordinate system
EBN	Energiebeheer Nederland
FDM	Finite Difference Method
FEM	Finite Element Method
KNMI	Koninklijk Nederlands Metereologisch Instituut
NAM	Nederlandse Aardolie Maatschappij
P	Primary wave
rms	root mean square
S	Secondary wave
SH	Secondary Horizontal wave
SV	Secondary Vertical wave

Chapter 1

Introduction

This work is part of an ongoing effort to understand the tremors in the Groningen field, their ground motions and effect on buildings. Recent results can be found in reports and presentations of NAM (2015), Stafleu et al. (2016), Bommer et al. (2015), Edwards et al. (2016), Bommer (2016), Burnett (2016) and van Dedem (2016) in relation to ground motion prediction equations (GMPE's), and of Dost and Kraaijpoel (2013), Dost (2016), Burnett (2016), Terrell (2016) and Lawrence et al. (2015) in relation to seismic moment tensor solutions of large tremors and the interpretation of tremors recorded by the down-hole geophones in the Zeerijp and Stedum wells in the Groningen field.

Essential for a further understanding of the source of the tremors in the Groningen field are the dimensions of the slip plane and the slip direction in relation to fault planes at or close to the tremor hypocentres. In this work, we try to derive the dimensions of the rupture plane of the relatively large Huizinge tremor from nearby ground motions. This tremor occurred at August 16^{th} 2012 and had a local magnitude $M_L = 3.6$. We use the tremor hypocentre location, fault orientation and slip direction proposed by KNMI.

Several features of seismic sources can be derived from the observed ground motions using analytical solutions for infinite uniform rock. However, full wave form simulations are needed to understand the effects of wave scattering in the various formations in the subsurface and of the slow down, bending and damping of the waves in the shallow subsurface, on the ground motions.
The model used is a kinematic model. It simulates the elastic waves resulting from a seismic source using the finite element method (FEM). The rupture plane of the seismic source is represented by one or a series of double couples along fault strike. The so-called source time function describes how the double couple forces develop over time. The elastic waves are calculated in a domain of several kilometres around the tremor hypocentre. This domain includes the locations of the nearby ground accelerometers of KNMI. The model uses realistic proxys for the geometries and wave velocities of the various formations in the overburden but not the slow down and relatively strong damping of the waves in the shallow subsurface. We assume that the relevant ground motion information is contained

in frequencies below about 5 Hz.

Chapter 2 presents the field data and the observed ground displacements following from the Huizinge tremor. Chapter 3 shows the FEM simulations results. A short discussion follows in Chapter 4. Appendix A shows field and ground accelerometer data. Appendix B shows results of additional simulations. Appendices C and D show details of the FEM simulations and basic relations between seismic moment, rupture plane dimensions and corner frequency.

Chapter 2

Field data used

2.1 Map and subsurface landscape

Figure 2.1 shows two maps of faults around the epicentre of the Huizinge tremor and the locations of several nearby ground accelerometers[1]. The left figure shows the major faults in the field from a NAM fault database. The right figure shows more faults with little throw and which have been recently found by Kortekaas and Jaarsma (2017) using fault plane tracking algorithms (or ant-tracking) on the seismic data of the Groningen field.
The red dots in both maps show the preferred location of the tremor epicentre. This location coincides with a junction of two faults with little throw. One fault has fault strike azimuth and fault dip angles $\phi \sim 330^\circ$ and $\delta \sim 68^\circ$, respectively. The fault strike azimuth angle is the angle between the Earth north direction and the fault strike where it is measured clockwise round from north, see also Figure C.1 in Appendix C. The other one has fault strike azimuth and fault dip angles $\phi \sim 265^\circ$ and $\delta \sim 82^\circ$, respectively[2].
The blue dots in the left figure show the locations of the ground accelerometers.

Figure 2.2 shows a perspective view of the lower horizons of a few formations in the overburden around the Huizinge tremor epicentre. Most horizons in the overburden formations are relatively flat like the one between the Chalk formation and the lower North Sea formation. The horizons of a thin anhydrite floater, which separates the lower and upper Zechstein formations, and the horizon between the upper Zechstein formation and the Triassic formation (not shown) have the largest variation in depth.
Small steps in the horizon between the Carboniferous underburden and the reservoir co-

[1]Using a regional velocity model and data from the regional borehole network, the KNMI calculated the epicentre in the Rijksdriehoeksstelsel (RD) coordinate system at X = 240.017 km and Y = 596.911 km. An improved epicentre location was obtained using a local model and including acceleration data from a network of 8 stations which are located within an epicentre distance of 2 - 10 km. This improved epicentre location is about 0.5 km west of the epicentre obtained using the regional model, see Dost and Kraaijpoel (2013). The RD coordinates are X = 239.519 km and Y = 597.095 km. In this report, the former location is called the original location and the latter one the preferred location.

[2]The large fault mapped by NAM, just east of the preferred tremor epicentre, has a fault strike azimuth $\phi \sim 166^\circ$ and a fault dip $\delta \sim 80^\circ$.

incide with faults in these formations. The throws of the faults near the Huizinge tremor epicentre are small to moderate, i.e. less than 30 metres. Further, the reservoir thickness around the tremor epicentre hardly varies.

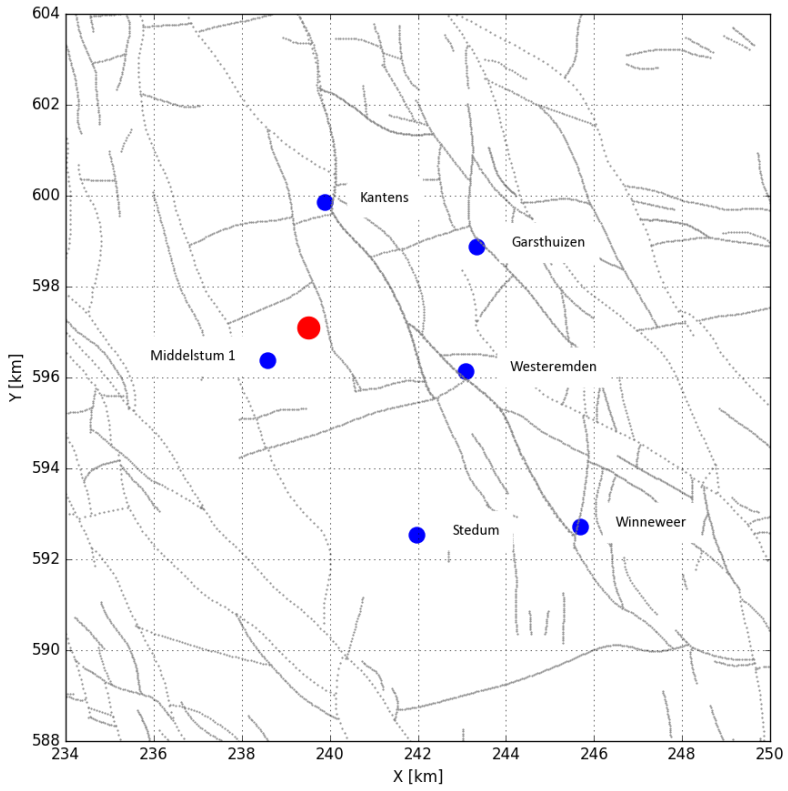

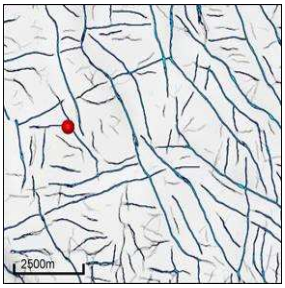

Figure 2.1 : Left figure: Faults and locations of preferred tremor epicentre (red dot) and ground accelerometers (blue dots) in the region around the Huizinge tremor in Dutch Rijksdriehoeksstelsel (DR) coordinates. The faults shown are from a NAM database that includes the fault dip, throw and azimuth angles. The thin grey dotted and solid fault lines shown are intersections of the faults with the top horizon of the Rotliegend reservoir. The preferred epicentre location of the tremor is from Dost and Kraaijpoel (2013).
The Middelstum-1, Westeremden, Kantens, Garsthuizen, Stedum and Winneweer ground accelerometers have been used by KNMI to determine the fault orientation and slip direction (or the focal sphere) of the tremor. The signals of the Middelstum-1, Westeremden and Kantens accelerometers are used in this report.

Right: Faults and location of preferred tremor epicentre (red dot) recently found by Kortekaas and Jaarsma (2017) from EBN using fault plane tracking algorithms (or ant-tracking) on seismic data.

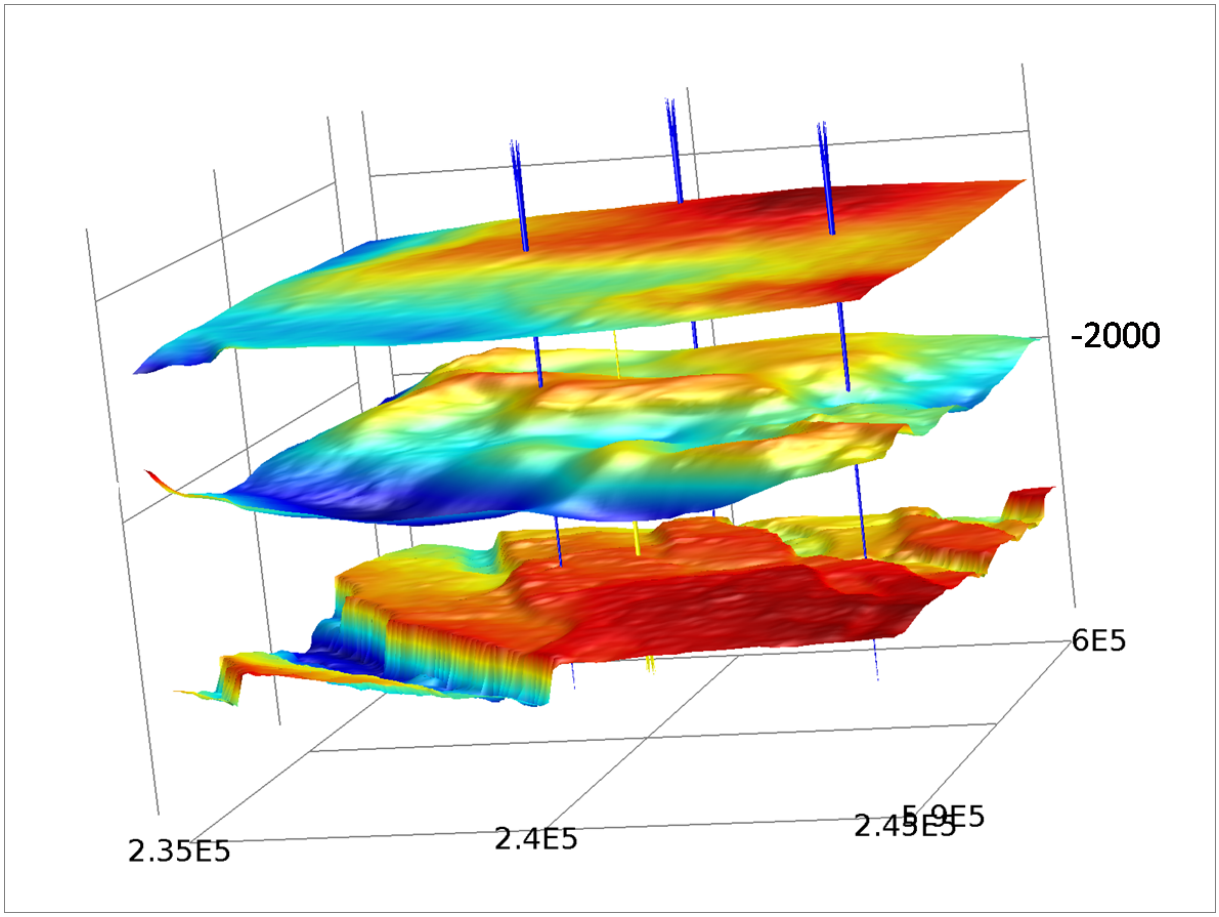

Figure 2.2 : A perspective view of three subsurface horizons of formations around the epicentre of the Huizinge tremor and ground accelerometers of interest. The horizons are the lower ones of the following formations: the reservoir (bottom), the Triassic formation (centre) and the Lower North Sea formation (top).
The domain shown is 10×10 km in horizontal dimensions. In the horizontal plane, the (X,Y) Dutch Rijksdriehoeksstelsel (DR) coordinates are in metres. Along the vertical axis, the depth in metres. The lower horizon of the Triassic formation is at about 2 km depth.
The location of KNMI's preferred epicentre is shown by the yellow upwards pointing needle. The tremor epicentre is located in the centre of a small horst with two small grabens west and east of it. The blue downwards pointing needles show the locations of the Middelstum-1, Westeremden and Kantens accelerometers. The horizons of the formations in the overburden have been mapped on a 25×25 m square grid and provided by NAM in the form of .csv files.

2.2 Accelerometer recordings

This work uses the displacements of the Middelstum-1, Westeremden and Kantens broadband accelerometers, see Appendix A for more data. These accelerometers are part of the

accelerometer surface network of the North Netherlands operated by KNMI. They were most close to the tremor epicentre and recorded the strong displacements from the direct body waves from the seismic source that propagated to the surface. For larger distances the source can be quite well represented by a point source and the lateral dimensions of the rupture plane can hardly be derived from the ground motions[3].

In general, the largest dimension of the rupture plane can be calculated from the corner frequency of the ground motions f_c [Hz] if the rupture velocity is known and the attenuation of the waves over the frequency range of interest is insignificant or can be included in the reconstruction of the source time function. For the Huizinge tremor, f_c = 2 - 2.5 Hz according to Dost and Kraaijpoel (2013). This more or less agrees with the intersection of the low- and high-frequency asymptotes of the displacement spectra and with the time period of the large oscillations in the displacements, see Appendix A. For rupture planes with large length to width ratio's, displacement spectra may show two corner frequencies related to both dimensions of the slip plane, see e.g. see Udias et al. (2014), §7.2 or Aki and Richards (2009), §10.1.5[4].
Assuming a rupture velocity V_r [m/s] of about 80% of the S wave velocity in the reservoir, a circular rupture plane would have a corresponding radius of about 0.3 km, see Appendix D, §D.2. From dynamic rupture modelling in the reservoir, we conclude that such a rupture velocity is possible for this magnitude. At the same time we cannot rule out that the rupture velocity was lower[5].

To obtain the fault plane orientation and slip direction, or the so-called focal sphere of the tremor, KNMI used also the Garsthuizen, Winneweer and Stedum accelerometer motions. The determination of the focal sphere is complicated because the accelerometer

[3]According to Udias et al. (2014), §4.1, a far distance in this context means that $s\lambda \gg L^2$ where $s = |\boldsymbol{x} - \boldsymbol{\zeta}_0|$ [m] is the distance between the epicentre of the source and the receiver. $\boldsymbol{x}$ [m] is the location of the receiver and $\boldsymbol{\zeta}$ [m] is the location of a surface element of the seismic source, L [m] is a typical dimension of the source and λ [m] is a dominant wavelength of the signal. The condition $s\lambda \gg L^2$ is explained by Aki and Richards (2009), §10.1.3.
For a 10 Hz wave with a wavelength $\lambda \sim 0.2$ km, and a source-receiver distance of 5 km, the point source approximation would be valid if $L \ll 1$ km. For a 2 Hz wave with a wavelength $\lambda \sim 1$ km, $L \ll 2$ km. Vice-versa, this means for this example that a source with a minimal dimension of about 1 km should be described as an extended source.
Dost and Kraaijpoel (2013) show also the Stedum ground accelerometer motions. This accelerometer is quite some distance away from the tremor epicentre and holds little information about the shape of the rupture plane.

[4]The spectra of the Westeremden accelerometer displacements suggest that there are two corner frequencies. The spectra of the Middelstum and Kantens accelerometers suggest one corner frequency, see Appendix A, Figure A.2 . Not more can be said before the effect of wave attenuation in the subsurface has been included in the analysis of the observed signals.

[5]Tremors generated in a similar reservoir setting in the Roswinkel field, south east from the Groningen field show a remarkably constant corner frequency over a wide range of tremor magnitudes $1.1 < M_L < 3.4$, see Dost et al. (2004). For these tremors, the so-called breakdown stress and/or rupture velocity seem to vary with the tremor magnitude. Again, not more can be said until the effect of wave attenuation has been included.

orientations in the horizontal plane are unknown. Despite this complication, plausible values for the fault strike azimuth, fault dip and rake angles have been derived[6]. They are $\phi = 320°$, $\delta = 80°$ and λ = -90°, respectively. For slip along fault dip with λ = -90° (or normal faulting), this means that the foot wall of the fault is on the west side of the fault. The proposed fault strike azimuth agrees with the signs of the vertical displacements during the arrival of the P wave, which do not depend on the accelerometer orientations.

The fault plane related to these parameters has a similar fault strike as one of the two faults identified by Energie Beheer Nederland (EBN), see Kortekaas and Jaarsma (2017). This one has a fault strike azimuth of 330°. The fault dip differs, the EBN one has a fault dip of about 68°.

The proposed slip direction along fault dip is also observed for a few other large tremors in the Groningen field by Dost (2016) although some other tremors in this field show slip directions with a significant component along fault strike, see Kraaijpoel and Dost (2013).

2.3 Seismic velocity model

The rock properties used are the rock density ρ [kg/m^3] and the primary (P) and secondary (S) wave velocities V_p and V_s [m/s] in the formations in the subsurface around the tremor epicentres. They originate from NAM's seismic velocity model which has been updated in 2015. Table A.2 in Appendix A shows the names of the formations for which the rock density and wave velocities have been defined by this velocity model and gives the mean depths of the formations below and above the reservoir in the region modelled.

Figure C.8 in Appendix C shows the profiles of the wave velocities over depth. In several formations, the wave velocities depend on depth. The seismic velocities in the 50 - 70 m thick anhydrite floater and anhydrite layer between the reservoir and the lower Zechstein formation are relatively high. Still, these formations scatter only a modest part of the energy of the low frequency waves of interest. The 1 - 5 Hz S waves have wavelengths which are substantially larger than the thicknesses of the anhydrite floater in the Zechstein and the anhydrite layer just above the reservoir. The low S wave velocity in

[6]The rake angle determines the slip direction of the rupture, see Figure C.1 in Appendix C.
The accelerometer orientations in the horizontal plane have been reconstructed by maximising the P wave energy in radial direction and the focal sphere has been based on a visual judgement of polarity plots. In these plots the accelerometer locations are corrected for refraction of the waves by the Zechstein salt and other formations in the overburden, see also Kraaijpoel and Dost (2013). Ray bending at the surface towards the vertical axis, because of the slow down of the waves in the shallow subsurface, is also included.
Usually, KNMI obtains the focal sphere from the computer programme Focmec which performs a systematic search of the focal sphere and reports acceptable solutions based on selection criteria for the number of polarity errors and errors in amplitude ratios. Input are the polarities (P, SV, SH) and/or amplitude ratios (SV/P, SH/P, SV/SH). The selection criteria for polarities and amplitudes allow correction or weightings for near-nodal solutions.

the shallow subsurface of the Upper North Sea formation has not been included in this velocity model.

Chapter 3

Finite element method simulations

A quick idea about ground motions from a point or extended seismic sources can be obtained from analytical solutions based on Green functions for wave propagation in infinite uniform rock. But, when the subsurface has various formations with different wave velocities, full wave propagation simulations are needed. Simulations based on finite difference methods are currently done by ExxonMobil and Shell to support the development of ground motion prediction equations (GMPE's) for the Groningen field, see van Dedem (2016), Burnett (2016), Terrell (2016), Lawrence et al. (2015) and Bommer (2016).

We assume in this report that the rupture starts on a fault plane in the reservoir at 3 km depth. The reservoir rock is assumed to be uniform and isotropic. The fault plane azimuth, dip angle and slip direction are those mentioned in §2.2. We focus on ground motions at the locations of the Middelstum-1, Westeremden and Kantens ground accelerometers. We disregard a dilatational component in the relative displacement of the rock along the fault although dynamic rupture modelling shows that the normal stress on the fault somewhat relaxes during rupturing. The domain of the simulations measures in the X, Y and Z-directions 9×10×6 km. It is centred around the original epicentre of the Huizinge tremor. The simulations use the velocity model 2015 of NAM for the various subsurface formations[1].

For local magnitudes $M_L \geq 2.5$, the moment magnitudes M are on average 0.2 units smaller than the local magnitudes reported by KNMI, see Dost et al. (2016). This means that the moment magnitude of the Huizinge tremor would be $M \sim 3.4$ on the scale of Richter and ground motions are reduced by a factor of about 2. On the other hand, ground motions during the passage of the S wave are amplified about twice because of the slow down of the S waves in the shallow subsurface. To include this amplification, the seismic moment M_0 of the tremor simulated is $M_0 = 300$ TJ[2].

[1]This model has been provided by Remco Romijn from NAM in the form of Excel and .csv files.

[2]The corresponding moment magnitude of the modelled tremor is $M = 3.55$ according to Kanamori's relation between seismic moment M_0 and moment magnitude M, i.e., $\log M_0 = 3/2M + 6.07$. It will be shown in following reports that the slow down and the relatively strong attenuation of waves in the

The FEM simulations are done with Comsol^{TM}. Like Diana^{TM}, this code can also include non-linear effects and can be used for dynamic rupture modelling which is useful for future studies. Details about the simulations, the implementation of the extended seismic source and a validation example are given in Appendix C.

3.1 Seismic source

A seismic source can be described as a point source or as an extended source. For a point source, the kinematics of the rupture process is completely defined by the so-called source time function. This function defines the relaxation of elastic forces on the slip plane as a function of time. In this case, the dimensions of the slip plane and the rupture velocity[3] are indistinguishable and implicitly included in the dynamics of the source time function.

For an extended source, the rupture velocity and the dimensions of the slip plane are explicitly included in the seismic source model. In general, the slip plane is divided in a number of relative small slip patches. For each slip patch a source time function is defined, which is in general a function of space and time. To model an extended source along fault strike, we have divided the rupture plane in a number of relative small slip patches along fault strike. The source time functions, representing the slip rate for each slip patch, are all the same except for a time shift. The time shift is defined by the rupture velocity, see §3.1.2.

3.1.1 Source time functions

We assume that the reservoir rock is uniform and isotropic and the slip is only deviatoric. For a receiver at a large distance from the seismic source, the source can be represented by a point source with a double couple or with a moment tensor[4]. The time dependent moment tensor $\boldsymbol{M} = \boldsymbol{M}(t)$ [N] can be factorised in a unit moment tensor $\boldsymbol{m}$ [-][5] and a source time function $M_0(t)$ [N]. The unit moment tensor $\boldsymbol{m}$ [-] is constructed from the unit vectors defining the orientation of the rupture plane and the slip direction, see e.g.

shallow subsurface lead to a ground motion amplification of about a factor 2 for the S wave and a delay in the arrival of the S wave at the surface of about 0.2 - 0.3 s, in agreement with Dost et al. (2004).

[3]The rupture velocity is the velocity with which the rupture front propagates over the slip plane.

[4]The source tensor provides fundamental information on the event magnitude, source geometry (e.g. possible fault plane orientations and slip directions), and partitioning among various deviatoric and isotropic motion components. If the reservoir rock is uniform and isotropic, the moment tensor and the so-called potency tensor differ only by a factor equal to the shear modulus μ, see for example Zhu and Ben-Zion (2013). One of the authors notes that, in general, it is better to use the strain-based potency tensor than the stress-based moment tensor, since the potency involves only directly observable quantities whereas the moment requires making assumptions on elastic properties at the source. In this case, this is not needed.

[5][-] means that the property, in this case $\boldsymbol{m}$ is dimensionless or has no unit.

Aki and Richards (2009), §3.3. So,

$$\boldsymbol{M}(t) = \boldsymbol{m} M_0(t). \tag{3.1.1}$$

If Brune's source time function would apply, which is often the case for natural earthquakes with equi-dimensional rupture planes, see Udias et al. (2014), Eq. 4.71,

$$M_0(t) = M_0 f_{stf}(t) \quad \text{where} \quad f_{stf}(t) = 1 - \big(1 + \frac{t}{t_r}\big) \exp(-t/t_r), \tag{3.1.2}$$

and

$$\dot{f}_{stf}(t) = \frac{t}{t_r^2} \exp(-t/t_r). \tag{3.1.3}$$

t_r [s] is the so-called rise time[6]. f_{stf} [-] is the dimensionless source time function. $\dot{f}_{stf}$ stands for the time derivative df_{stf}/dt. For $t \gg t_r$, $f_{stf} \to 1$. M_0 [N] is the seismic moment.

Using the mean relative displacement or slip $D = D(t)$ over the slip plane as the time-dependent variable and the general relation between slip and seismic moment $M_0 = \mu S D$, the seismic moment changes with time as

$$M_0(t) = \mu S D(t) = M_0 f_{stf}(t) \quad \text{where} \quad D(t) = D_{max} f_{stf}(t) \quad \text{and} \quad M_0 = \mu S D_{max}. \tag{3.1.4}$$

D_{max} [m] is the maximum value of the mean slip over the slip plane over time. S [m^2] is the surface of the slip plane and μ [Pa] the shear modulus of the rock.

When a rupture along fault dip is limited to an area of high shear stress in the reservoir, two-dimensional dynamic rupture modelling indicates that the decay of the mean slip velocity over the fault is faster than would correspond with the exponential tail in the Brune source time function. The following modified source time function corresponds with this behaviour, i.e.[7]

$$\dot{f}_{stf}(t) = c_{stf} g(t) \frac{t}{t_r^2} \exp(-(t/t_r)^n) \quad \text{where} \quad g(t) = \frac{t^2}{t^2 + t_{onset}^2}. \tag{3.1.5}$$

n [-] is a shape parameter which determines the decay time of $\dot{f}_{stf}$. c_{stf} [-] is a constant, so that $f_{stf} \to 1$ for $t \gg t_r$. The function $g(t)$ ensures that $f_{stf}(t)$ has a zero second order time derivative at $t = 0$, which is convenient for the numerical simulations. t_{onset} [s] is a typical time in which $g(t)$ increases from 0 to 1. Using $t_{onset} \ll t_r$, $g(t)$ has a minimum effect on the main shape of the source time function.

[6] For the Brune source time function, the rise time t_r relates to the corner frequency f_c as $t_r \sim 1/(2\pi f_c)$.

[7] This empirical function differs from other source time functions used in the literature, see for example Beresnev and Atkinson (1997).

Figure 3.1 shows examples of the source time functions used in this report. The modified one with the longer rise time, $t_r = 0.2$ s, is used to model ruptures in equi-dimensional rupture planes. The modified one with the shorter rise time $t_r = 0.08$ s is used for ruptures along fault strike.

3.1.2 Seismic source size

The first seismic source used has a ribbon-like rupture plane along fault strike. It is represented by a series of double couples with a double couple arm $l_{DC} = 80$ m over a length L of about 1 km, see Appendix C for details[8]. The rupture starts at the source centre and propagates in both horizontal directions along fault strike with a rupture velocity $V_{r,strike}$ = 2 km/s, which is 80 - 90% of the S wave velocity in the reservoir[9]. The external source model resembles Haskell's model for an extended source, see e.g. Udias et al. (2014), §7.2 or Aki and Richards (2009), §10.1.5.

The source time function for double couple i in this series of double couples is

$$f_{stf}(t) = c_{stf} g(t^*) \frac{t^*}{t_r^2} \exp(-(t^*/t_r)^n), \tag{3.1.6}$$

where $t^* = 0$ for $t < t_{trigger}$ and $t^* = t - t_{trigger}$ for $t \geq t_{trigger}$ and the trigger time $t_{trigger}$ [s] is given by[10]

$$t_{trigger} = \frac{|\boldsymbol{\zeta}_i - \boldsymbol{\zeta}_{nucl}|}{V_{r,strike}}. \tag{3.1.7}$$

$|\boldsymbol{\zeta}_i - \boldsymbol{\zeta}_{nucl}|$ is the distance between double couple i and the source centre where the rupture starts. $V_{r,strike}$ [m/s] is the rupture velocity along fault strike.
The modified source time function used has shape parameters $t_r = 0.08$ s, $n = 2$. For these parameters, the time in which the rupture propagates along fault dip is about 0.15 s, see Figure 3.1 . This time is sufficient to propagate over a depth of about 0.3 km in

[8]The length L [m] of the source along fault strike follows from the relation between the seismic moment of the tremor M_0 [N] and the stress drop $\Delta\tau$ [Pa], see Appendix D, Eq. (D.1.4),

$$L \sim \left(\frac{8}{3\pi W} \frac{M_0}{\Delta\tau} \right)^{1/2}.$$

W [m] is the width of the rupture plane along fault dip. M_0 is the sum of the seismic moments released by all double point sources.

[9]The rupture velocity is the velocity with which the rupture front propagates along the fault plane. It essentially differs from the so-called slip velocity. The latter is the relative velocity with which one plane along the fault moves with respect to the other plane. The slip velocity is usually in the order of 1 m/s and is determined by stress breakdown and rock inertia.

[10]With a focus on the low-frequency content of the simulated waves, we disregard possible irregularities in the rupture velocity along fault strike due to fault plane and stress heterogeneities. To include them, see for example Graves and Pitarka (2010) or Graves and Pitarka (2015).

one direction for a rupture velocity $V_r = 2$ km/s.

The second seismic source used is represented by one or two double couples at the source centre with a double couple arm $l_{DC} = 80$ m. This source can be regarded as a point source but with a source time function applicable for a rupture in an equi-dimensional plane of considerable dimensions. Using the modified source time function with shape parameters $t_r = 0.2$ s, $n = 2$, the time in which the rupture propagates is about 0.25 s. This corresponds with a rupture propagation over a radius of about 0.5 km for a rupture velocity $V_r = 2$ km/s.

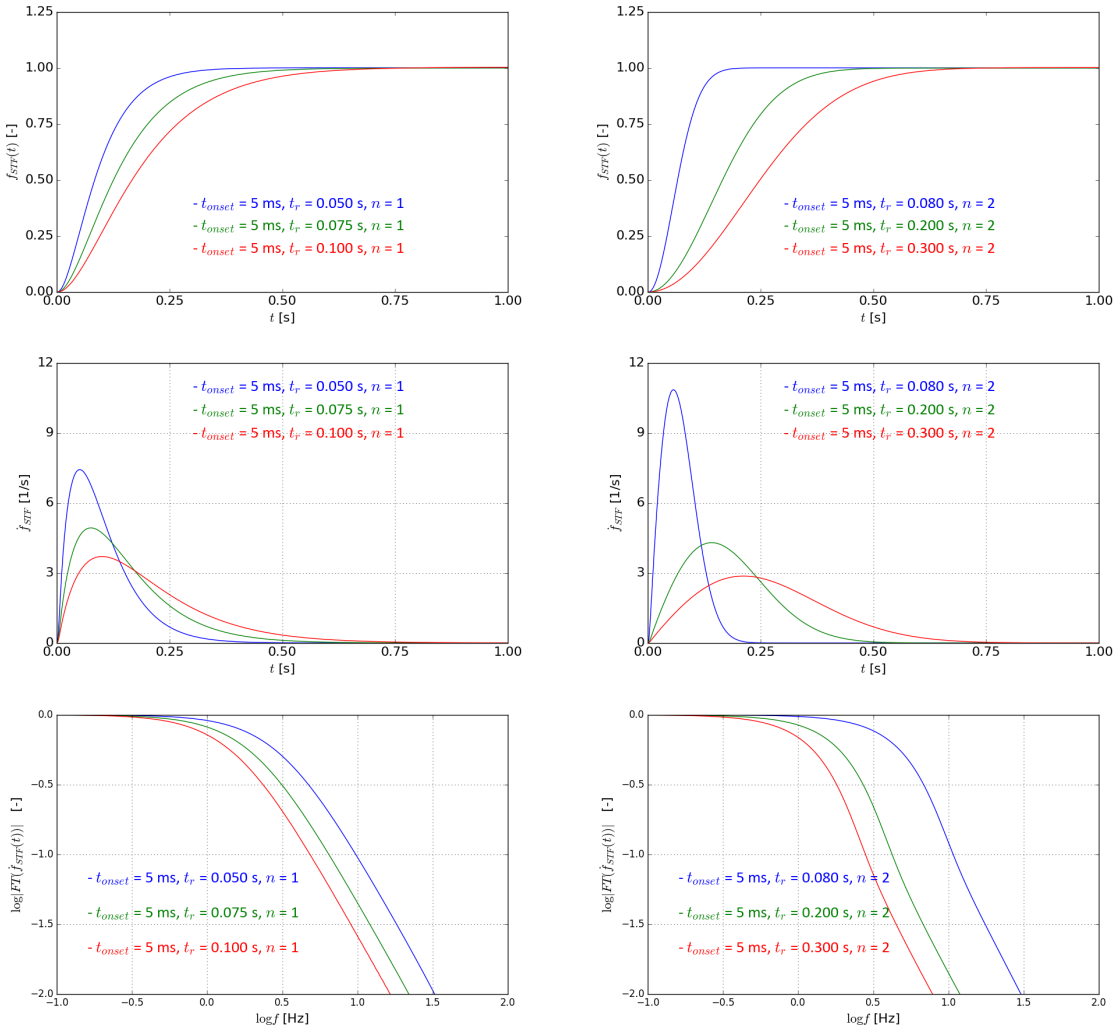

Figure 3.1 : Source time functions $f_{stf}(t)$ (top), time derivatives $\dot{f}_{stf}(t)$ (centre) and absolute values of the logarithm of the Fourier transforms of the time derivatives $\log^{10}|F(\dot{f}_{stf}(t))|$ (bottom) used in the FEM simulations.
Left: the Brune source time function, Eq. (3.1.2) with shape parameter $t_r = 0.05$ s (blue), 0.075 s (green) and 0.1 s (red). The corresponding corner frequencies are 3.1, 2.1 and 1.5 Hz, respectively.
Right: modified source time function, Eq. (3.1.5) with shape parameters $n = 2$ and $t_r =$ 0.08 s (blue), 0.2 s (green) and 0.3 s (red). The corresponding corner frequencies are 5.2, 2.1 and 1.4 Hz, respectively.
The corner frequency is the frequency for which the amplitude of the Fourier transform is half the maximum value. For the Brune source time function, the rise time t_r relates to the corner frequency f_c as $t_r \sim 1/(2\pi f_c)$. The high-frequency asymptote of the amplitude spectrum is proportional with f^{-2}.
The modified source time function has for the same rise time t_r a faster decay than the Brune source time function, in line with results obtained from dynamic rupturing. The frequency spectra show a much faster initial decay than the Brune source time function, i.e. the initial decay is with about a power f^{-3} instead of a part of a gradual transition to f^{-2}.
In all cases, the small onset time $t_{onset} = 5$ ms has a negligible effect on the shapes of the curves.

3.2 Results

Figure 3.2 shows the observed and simulated accelerometer displacements using the proposed fault orientation and slip direction. In addition to the first order 0.1 Hz high-pass filter of the accelerometer datalogger system, the observed displacements have been filtered using a 0.3 Hz high-pass regression filter. The simulated displacements have been filtered in a similar way. The unfiltered displacements are shown in Appendix B. The observed and simulated displacements show amplitudes of similar order and shape. The high frequency asymptotes of the spectra of the simulated displacements depend on the frequency roughly as f^{-3} in agreement with the high frequency asymptote of the spectrum of the source time function used and the observed spectra, see Appendix B, Figure B.2 . There are also differences. These are

- The calculated ratio between the vertical and radial displacement amplitudes (or P/SV ratio) is higher than observed. In particular, the simulated vertical displacements are stronger than observed.
- The calculated ratio between the transverse and radial displacement amplitudes (or SH/SV ratio) is smaller than observed.
- The calculated radial displacements show relatively slow gradual changes unclear in the observed displacements.
- The simulations do not reproduce the observed double peaks in the radial displacements, clearly observed for the Middelstum-1 and Kantens accelerometers. A source time function which would represent two ruptures within about 0.5 s is a possibility to explain the observed displacements. If so, the calculated ground motions should also be consistent with the observed ones for the Westeremden and other accelerometers.
- The calculated time difference between the arrivals of the P and S waves is about 0.2 s smaller than observed. This difference is due to the slow down of S wave in the shallow subsurface.

Part of the differences can be explained by wave bending in the shallow subsurface towards the vertical axis. Another explanation is that the fault plane and/or slip direction or tremor hypocentre are different than proposed. Figures B.4 - B.6 in Appendix B show how ground motions vary with the fault dip angle and slip direction.

One of the reasons that the simulated vertical displacements are stronger than observed is due to the amplification of the simulated ground motions by a factor two. This amplification is done in the simulations to include the effect of the slow down of the S waves in the shallow subsurface. In reality, the compressional P waves hardly slow down in the shallow subsurface and, as a consequence, the ground motions from these waves, which are primarily vertical, should not be amplified by a factor 2.

The relatively slow gradual changes in the simulated radial displacements are so-called near field contributions of the seismic waves. They even remain after high-pass filtering comparable with the filtering of the observed signals. The effect of the high-pass filters is shown in Figure B.1 in Appendix B. It is not clear yet why the slowly gradual changes are almost invisible in the observed displacements.

Similar simulations have been done for an equi-dimensional source of limited size and represented by a point source. The displacement peaks for the equi-dimensional source are smoother but differences are subtle, see Figure B.3 in appendix B[11]. Considering the present uncertainty in the horizontal orientations of the accelerometers, it is too early to judge which rupture plane shape would be more likely.

[11]Depending on the accelerometer location, the displacement signals from an extended source along fault strike show a peak and a plateau. The peak follows from the arrival of waves which originate from the rupture front along fault strike propagating in the same direction. The plateau follows from the arrival of waves from the rupture front along fault strike propagating in the opposite direction.

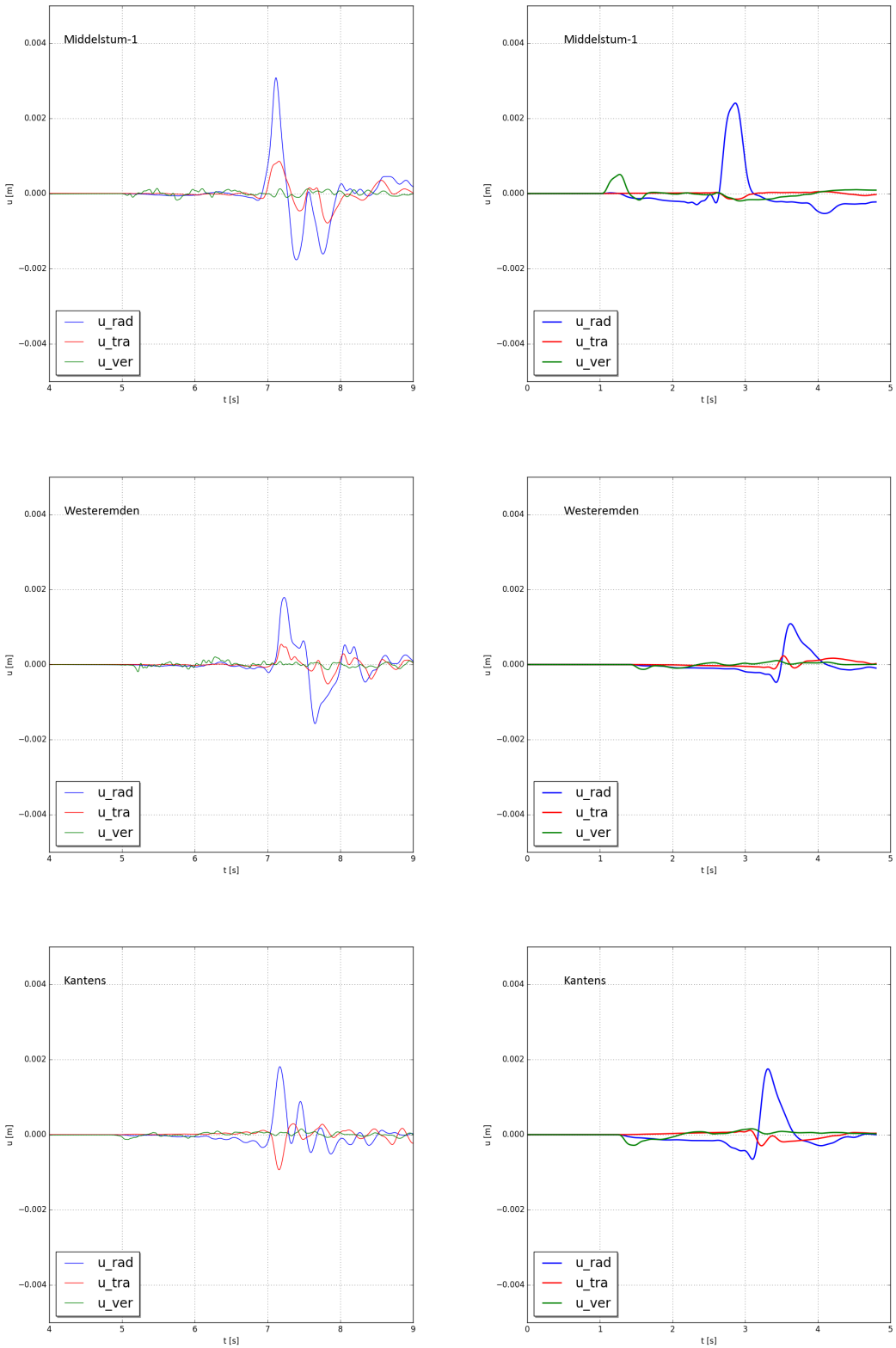

Figure 3.2 : Observed (left) and simulated (right) displacements of the Middelstum-1, Westeremden and Kantens accelerometers following from the Huizinge tremor.
The blue, red and green curves show the radial, transverse and vertical displacements u_{rad}, u_{tra} and u_{ver}, respectively. The centre of the extended source is located at 3 km depth at the original location of the epicentre of the Huizinge tremor. The seismic source is a ribbon-like source along fault strike. The absolute value of the time of the observed signals has no meaning.

Chapter 4

Discussion

There is a fair correspondence but there are also significant differences between the observed and simulated displacements of the Huizinge 2012 tremor using the proposed values for the orientation of the fault plane and slip direction. Since these values also depend on the orientation of the accelerometers in the horizontal plane, which is unknown, further work is needed to decide whether other fault plane orientations and slip directions are also possible. In particular, we want to know whether slip may have occurred on the other fault identified by EBN near the Huizinge tremor epicentre.

To reconstruct the shape of the rupture plane of relatively large tremors in the Groningen field, the simulations confirm that this can only be done when the ground accelerometers are sufficiently close to the tremor epicentre and the tremors in the Groningen field are substantial. Still, differences in the ground displacements due to the shape of the rupture plane are subtle and can only be used to reveal the rupture plane when there is more certainty about the fault orientation and slip direction.

This first comparison between observations and simulations suggest that the two oscillations don't arise from multiple scattering of waves in the overburden. One possibility is that they follow from two ruptures not far apart in distance and occurring within 0.5 s after each other[1]. To confirm or reject this possibility additional simulations are needed. These should also address a comparison between modelled and observed ground motions for the other accelerometers[2].

[1] If so, the differences between peak times recorded by the ground accelerometers could be used to locate the centre of the second rupture with respect to the first one. Since the start of the second rupture with respect to the start of the first one is unknown, at least four accelerometers must record these two peaks. Assuming that one or two of coordinates of the hypocentre of the second rupture are known the number of accelerometers could be reduced. Ray tracing techniques which include the refraction of the waves in the overburden, could be a straightforward way to derive this location. We will try this once remaining uncertainties in the derivation of the source mechanism are resolved.

[2] In general, the shape of the ground motion signals, and herewith the strength of appearance of a second peak, vary with the location of the accelerometer with respect to the source, see e.g. an example of signals from a complex source in Udias et al. (2014), Figure 8.9. for the Chili 2010 earthquake.

The reconstruction of the accelerometer orientations in the horizontal plane and a possible improved inclusion of wave attenuation in the subsurface will be part of another report. This work will also include the analysis of the ground motions recorded by the Stedum, Garsthuizen and Winneweer accelerometers.

Chapter 5

Acknowledgements

I thank Remco Romijn and Clemens Visser from NAM for providing me the field data and the velocity model, Marloes Kortekaas from EBN for providing me new faults close to the preferred Huizinge tremor epicentre and Bernard Dost from KNMI for providing me the accelerometer data and a plausible fault orientation and slip direction and many suggestions. I thank Nora DeDontney, Will Burnett and Grant Gist from ExxonMobil and Steve Oates, Xander Campman and Ewoud van Dedem from Shell Global Solutions for other comments and suggestions.

Bibliography

Aki, K., and Richards, P. G., "Quantitative Seismology", University Science Books, 2009.

Beresnev, I. A., and Atkinson, G. M., "Modelling Finite-Fault Radiation from the ω^n Spectrum", Bull. Seis. Soc. Am., 87, 67–84, 1997.

Bommer, J. J., Dost, B., Edwards, B., Rodriguez-Marek, A., Kruiver, P., Meijers, P., Ntinalexis, M., and Stafford, P. J., "Development of Version 2 GMPEs for Response Spectral Accelerations and Significant Durations from Induced Earthquakes in the Groningen Field",, Technical report, Nederlandse Aardolie Maatschappij B.V., the Netherlands, 2015.

Bommer, J. J., "Overview of Development of Current Ground-Motion Model for the Groningen Field",, Technical Report presentation for Groningen GMPE Workshop, London, 18-20 July 2016, Independent consultants to NAM, 2016.

Burnett, W., "3D Finite Difference Wavefield Modeling for Ground Motions",, Technical Report presentation for Groningen GMPE Workshop, London, 18-20 July 2016, ExxonMobil URC, Houston, 2016.

Dost, B., and Haak, P. J., "A Comprehensive Description of the KNMI Seismological Instrumentation",, Technical Report Technical report TR-2452002, Koninklijk Nederlands Metereologisch Instituut, the Netherlands, 2002.

Dost, B., and Kraaijpoel, D., "The August 16, 2012 Earthquake near Huizinghe (Groningen)",, Technical Report KNMI report TR 16/1/2013, Koninklijke Nederlands Meteorologisch Instituut, the Netherlands, 2013.

Dost, B., van Eck, T., and Haak, H., "Scaling of Peak Ground Acceleration and Peak Ground Velocity Recorded in the Netherlands", Bollettino di Geofisica Teorica ed Applicata, 45, 153–168, 2004.

Dost, B., Edwards, B., and Bommer, J. J., "Local and Moment Magnitudes in the Groningen field",, Technical Report unpublished report, 4 March 2016, Koninklijke Nederlands Metereologisch Instituut, Netherlands, 2016.

Dost, B., "Moment Tensor Solutions for Groningen Earthquakes",, Technical Report presentation for Groningen GMPE Workshop, London, 18-20 July 2016, Koninklijke Nederlands Metereologisch Instituut, Netherlands, 2016.

Edwards, B., Bommer, J., Stafford, P., and Rodrigues-Marek, A., "Inversion of Ground Motions for Source, Path and Site Parameters and Generation of Stochastic Records",, Technical Report presentation for Groningen GMPE Workshop, London, 18-20 July 2016, Independent consultants to NAM, 2016.

Graves, R. W., and Pitarka, A., "Broadband Ground-Motion Simulation using a Hybrid Approach", Bull. Seis. Soc. Am., 100, 2095–2133, 2010.

Graves, R. W., and Pitarka, A., "Refinements to the Graves and Pitarka (2010) Broadband Ground-Motion Simulation Method", Seismological Research Letters, 86, 1–6, 2015.

Hanks, T. C., and Kanamori, H., "A Moment Magnitude Scale", J. of Geophys. Res. Solid Earth, 84, 2348–2350, 1979.

Kortekaas, M., and Jaarsma, B., "Improved Definition of Faults in the Groningen Field using Seismic Attributes", submitted to Netherlands Journal of Geosciences, -, –, 2017.

Kraaijpoel, D., and Dost, B., "Implications of Salt-related Propagation and Mode Conversion Effects on the Analysis of Induceed Seismicity", Journal of Seismology, 17, 95–107, 2013.

Lawrence, Z., Gans, C., Bailey, J., Burnett, W., Gist, G., and Reilly, J., "Groningen Seismic Observations and Independent Event QC",, Technical Report presentation for NAM/URC Groningen Workshop, 4-6 March 2015, ExxonMobil URC, Houston, 2015.

Leonard, M., "Earthquake Fault Scaling: Self-Consistent Relating of Rupture Length, Width, Average Displacement, and Moment Release", Bull. of the Seism. Soc. of America, 100, 1971–1988, 2010.

NAM, "Geological Schematisation of the Shallow subsurface of Groningen for Site Response to Earthquakes for the Groningen gas field, Deltares report",, Technical report, Nederlands Aardolie Maatschappij B.V., the Netherlands, 2015.

Scholz, C. H., "The Mechanics of Earthquakes and Faulting, 2^{nd} edition", Cambridge University Press, 2002.

Stafleu, J., Gunnink, J., de Lange, G., and Kruiver, P., "Shear Wave Velocity for the Upper 30 m - Combining the GeoTOP 3D Voxel Model and Seismic CPT's",, Technical Report presentation for workshop SoDM, 17 march 2016, TNO, Utrecht, Houston, 2016.

Stein, S., and Wysession, M., "An Introduction to Seismology, Earthquakes, and Earth Structure", Blackwell Publishing, 2003.

Terrell, M., "Structural Overview and Max Magnitude Summary",, Technical Report presentation for Groningen GMPE Workshop, London, 18-20 July 2016, ExxonMobil URC, Houston, 2016.

Udias, A., Madariaga, R., and Buforn, E., "Source Mechanisms of Earthquakes - Theory and Practice", Cambridge University Press, 2014.

van Dedem, E. J., "Ground Motion Modeling for Groningen",, Technical Report presentation for Groningen GMPE Workshop, London, 18-20 July 2016, Shell Global Solutions International, Rijswijk, 2016.

Zhu, L., and Ben-Zion, Y., "Parametrization of General Seismic Potency and Moment Tensors for Source Inversion of Seismic Waveform Data", Geophys. J. Int., 194, 839843, 2013.

Appendix A

Field data and accelerometer data

Appendix A.1 Tremor and ground accelerometer coordinates

Table A.1 shows the Rijksdriehoeksstelsel (RD) coordinates of the tremor and ground accelerometers of interest. Some simulations have been done using the original location of the Huizinge tremor, see Dost and Kraaijpoel (2013). Using a regional velocity model and data from the regional borehole network, the KNMI calculated the epicentre at: X = 240.017 km and Y = 596.911 km. An improved epicentre location was obtained using a local model and including acceleration data from a network of 8 stations that are located within an epicentre distance of 2-10 km. This location lies about 0.5 km west of the epicentre obtained using the regional model at X = 239.519 km and Y = 597.095 km. In this report, the former location is called the original location and the latter one the preferred location.

Table A.2 shows the names of the formations used in the seismic velocity model 2015 and the mean, maximal and minimal depths of the lower horizons of these formations in the region around Huizinge. Table A.3 shows the rock types in these formations.

Table A.1 : The Dutch Rijksdriehoeksstelsel (DR) coordinates of the preferred and original epicentres of the Huizinge tremor and the KNMI accelerometers used.

Name	KNMI station	ser. no.	date	M_L	X	Y
				Richter	km	km
tremor						
Huizinge (preferred)			2012-08-16	3.6	239.519	597.095
Huizinge (original)				3.6	240.017	596.911
ground accelerometers						
Middelstum-1	NL.BMD1	401			238.581	596.379
Westeremden	NL.BWSE	834			243.091	596.144
Stedum	NL.BSTD	117093			241.973	592.547
Kantens	NL.KANT	115275			239.881	599.868
Garsthuizen	NL.GARST	115282			243.327	598.884
Winneweer	NL.WIN	115277			245.681	592.717

Table A.2 : Mean depths of the lower horizons of the formations around the Huizinge tremor which are used in the seismic velocity model of NAM, update 2015 in a 10×10 km area defined by the following DR coordinates: X_{min} = 235 km, X_{max} = 245 km and Y_{min} = 590 km, Y_{max} = 600 km.
Further, the table shows the mean thicknesses of these formations and the standard deviation, minimum and maximum values of the depths of the lower horizons. The minimum and maximum values are averages in square grid cells of 500×500 m.

Formation name used	mean depth lower horizon m	mean thickness m	stdev lower horizon m	min. value lower horizon m	max. value lower horizon m
Upper North Sea	-350	350	26	-495	-315
Lower North Sea	-850	500	44	-961	-764
Chalk	-1690	840	56	-1837	-1509
Rijnland	-1775	85	57	-1930	-1571
Altena	-	-	-	-	-
Triassic	-1935	60	103	-2199	-1765
upper Zechstein	-2178	143	154	-2526	-1781
floater	-2225	47	164	-2633	-1815
lower Zechstein	-2825	600	98	-3178	-2706
anhydrite	-2876	51	98	-3230	-2750
Rotliegend reservoir	-3144	268	104	-3506	-3002
Carboniferous underburden	< -6000				

Table A.3 : Rock type of the formations in the 2015 seismic velocity model of NAM.

Formation name used	rock type
Upper North Sea	Quarternary shallow marine to terrestial clay and fine to course sands
Lower North Sea	Tertiary shallow marine clays, sands and sandstones
Chalk	Cretaceous shallow to deep-marine limestone
Rijnland	Cretaceous shallow marine marlstone, claystone and interbedded sandstones
Altena	Jurassic marine claystone
Triassic	Triassic lower Bundsandstein formation: lacustrine claystone, siltstone and very fine sandstone
upper Zechstein	Zechstein evaporite, rock salt
floater	Zechstein floater, anhydrite
lower Zechstein	Zechstein evaporite, rock salt
anhydrite	Anhydrite and dolomite
Rotliegend reservoir	Ten Boer claystone - lacustrine shale with thin sandstone Slochteren sandstone reservoir - mixed fluvial-aeolian sandstone
Carboniferous underburden	lacustrine and floodplain siltstones, organic shales and lower delta plain fine sandstones

Appendix A.2 Ground accelerometer recordings

The accelerometers which recorded the Huizinge tremor were SIG AC-23 broadband accelerometers from GeoSIG^{TM} (Switzerland) in combination with data loggers. They have been part of the accelerometer surface network of the North Netherlands, operated by KNMI[1]. The main purpose of these accelerometers was to determine the tremor hypocentres and the peak ground accelerations. The polarity of the signals was in these years of less interest. In the following, we show the accelerations and velocities and the focal mechanism according to the latest processing by KNMI. These signals differ from those shown in Dost and Kraaijpoel (2013). From these signals we have derived auto-correlation functions of the displacement velocities, Fourier transforms of the displacements and the accelerometer motions (or so-called particle motions) in the horizontal plane.

Figure A.1 shows the horizontal radial, transverse and vertical displacements and accelerations of the accelerometers. The former result from integrating the latter. Since the orientation of the accelerometers in the horizontal plane during the recording of the Huizinge tremor is unknown, a fundamental uncertainty about the horizontal (radial and transverse) components remains.
The vertical S wave amplitudes are smaller than the horizontal ones. The P wave amplitudes are smaller than the S wave ones. The radial displacement of the Middelstum-1 accelerometer following from the Huizinge tremor shows two distinct low-frequency oscillations.

Figure A.2 shows the absolute values of the Fourier transforms (or frequency spectra) of the displacements and the so-called horizontal particle motions. The spectra have a more or less flat low-frequency asymptote below 1 Hz and a high-frequency asymptote above 3 Hz which decays with f^{-n} with $n \sim 3$ for the Middelstum-1 and Kantens accelerometers. This decay follows from the rupture process dynamics (or source time function used) and frequency dependent wave attenuation in the subsurface. Further, it can be changed by

[1]These 0.1 Hz - 100 Hz accelerometers have a temperature stability of 1 mV/°C at a full scale output of ± 10 V. The full scale corresponds to ± 0.1, 0.2, 0.5, 1, 2 and 4 g depending on jumper settings. The damping of the sensor is 'critical' with damping factor 0.7. The dynamic range is 125 dB. The sample frequency is 200 Hz. According to Dost and Haak (2002), §6, the bandwidth of the sensor is characterised by one pole (or first order) high-pass filter at 0.1 Hz and by a 2 pole (or second order) Bessel low-pass filter at 50 Hz. The signals have been sampled through a digital Hogenauer filter with a 3 dB point at 52 Hz. The result of these filters is a practically flat system response between 0.3 and 10 Hz and a steep fall off above 30 Hz, see Figure 6.2 in the aforementioned reference.
For accelerometers with 3 digit serial numbers, the sign of the vertical signal is positive in downwards direction. For accelerometers with 6 digit serial numbers, the sign of the vertical signal is positive in upwards direction, see Table A.1 . In this report the signs of the vertical signals have been converted. For all accelerometers the sign is positive when the displacement is in upwards direction.
After 2012, the SIG AC-23 sensors have been replaced by EpiSensor^{TM} broadband DC - 200 Hz accelerometers from Kinemetrics, Inc., CA (US). For this reason, the orientation of the accelerometers in the horizontal plane cannot be checked anymore.

the instrument response, data logging and signal processing[2].
The decay is comparable with high-frequency asymptote of the modified source time function we have used in the simulations, see §3.1.1 but note that a possible frequency dependent wave attenuation in the subsurface has not been considered yet.

Corner frequencies, as derived from intersections of the low-frequency and high-frequency asymptotes of the displacement spectra, somewhat vary[3]. They agree with the range of corner frequencies given by Dost and Kraaijpoel (2013). Before saying more about the observed ground motion spectra, the effect of wave attenuation in the subsurface on the observed motions need to be included.

The accelerometer motions in the horizontal plane, which can be derived from the radial and transverse displacements, depend on the fault plane orientation and slip direction. Figure A.3 shows the projection of the main horizontal accelerometer motions in the horizontal plane on a map.

[2]In our case, the fall-off for frequencies < 0.3 Hz is a result of the regression filter used by KNMI when processing the data. The high-frequency decays in the spectra are well below 30 Hz above which the receiver system response steeply falls off.

[3]For the horizontal displacements, these values agree also with those of dominant time shifts in the auto-correlation functions of the displacement velocities. For the Middelstum-1 and Kantens accelerometers, the first non-zero time shifts of positive peaks in the radial and transverse displacement velocity correlation functions are $t_{shift} = 0.4$ - 0.45 s and $t_{shift} \sim 0.3$ s, respectively. These values correspond with dominant frequencies of 2.2 - 2.5 Hz and ~ 3 Hz, respectively. For the spectra of the Westeremden accelerometer displacements, intersections between the high- and low-frequency asymptotes are less clear. According to the displacement velocity auto-correlation function, $t_{shift} \sim 0.3$ s, corresponding with a dominant frequency of ~ 3 Hz.
The spectra of the vertical displacements somewhat differ from the horizontal ones, especially for the Westeremden accelerometer. The vertical spectra contains a significant contribution from the P wave while the horizontal ones primarily contain contributions from the S wave.

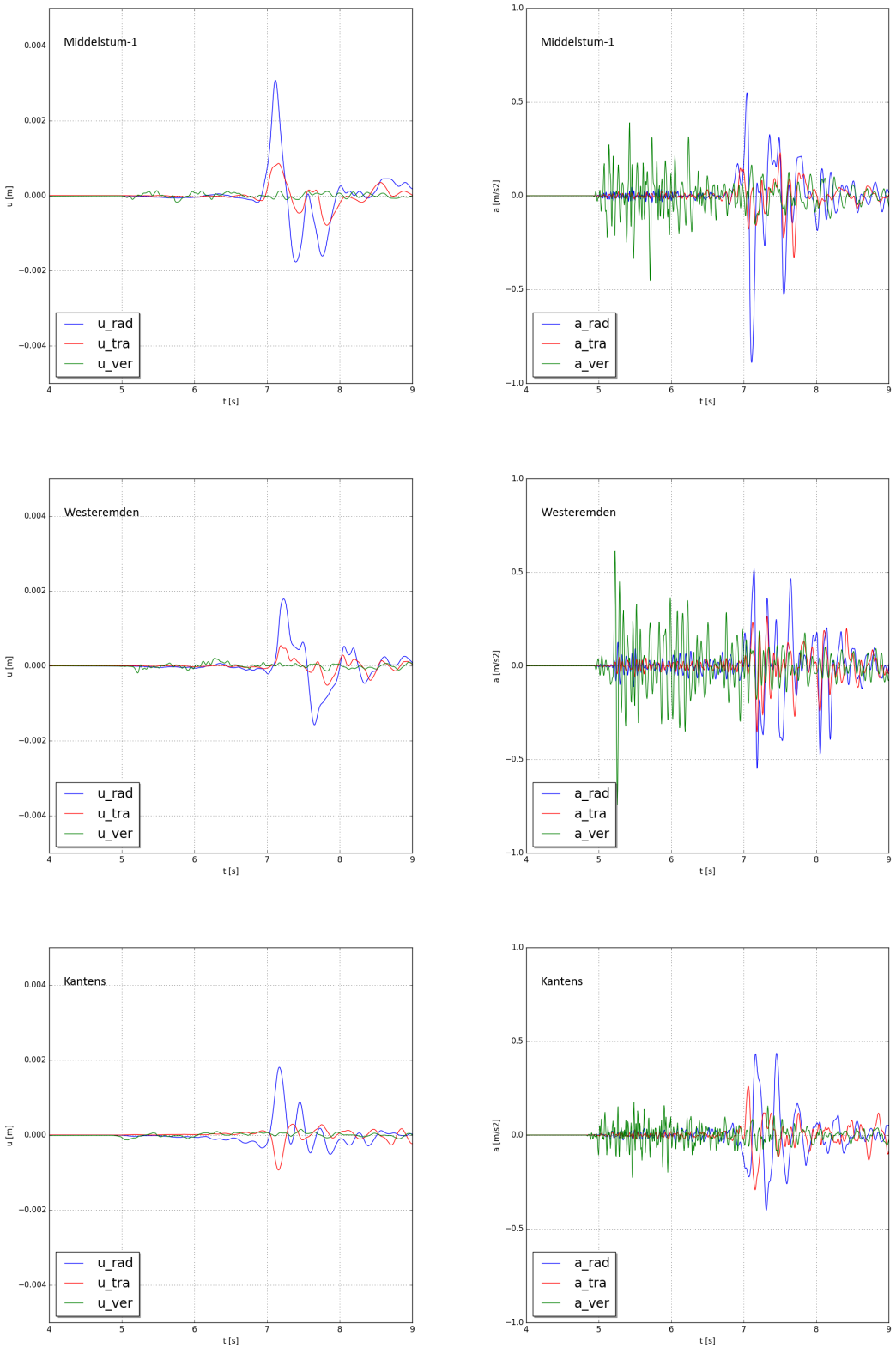

Figure A.1 : Displacements (left) and accelerations (right) of the Middelstum-1, Westeremden and Kantens accelerometers (from top to bottom) following from the Huizinge tremor. The signals originate from KNMI.
The blue, red and green curves show the radial, transverse and vertical displacements, u_{rad}, u_{tra} and u_{ver} and corresponding accelerations a_{rad}, a_{tra} and a_{ver}, respectively.

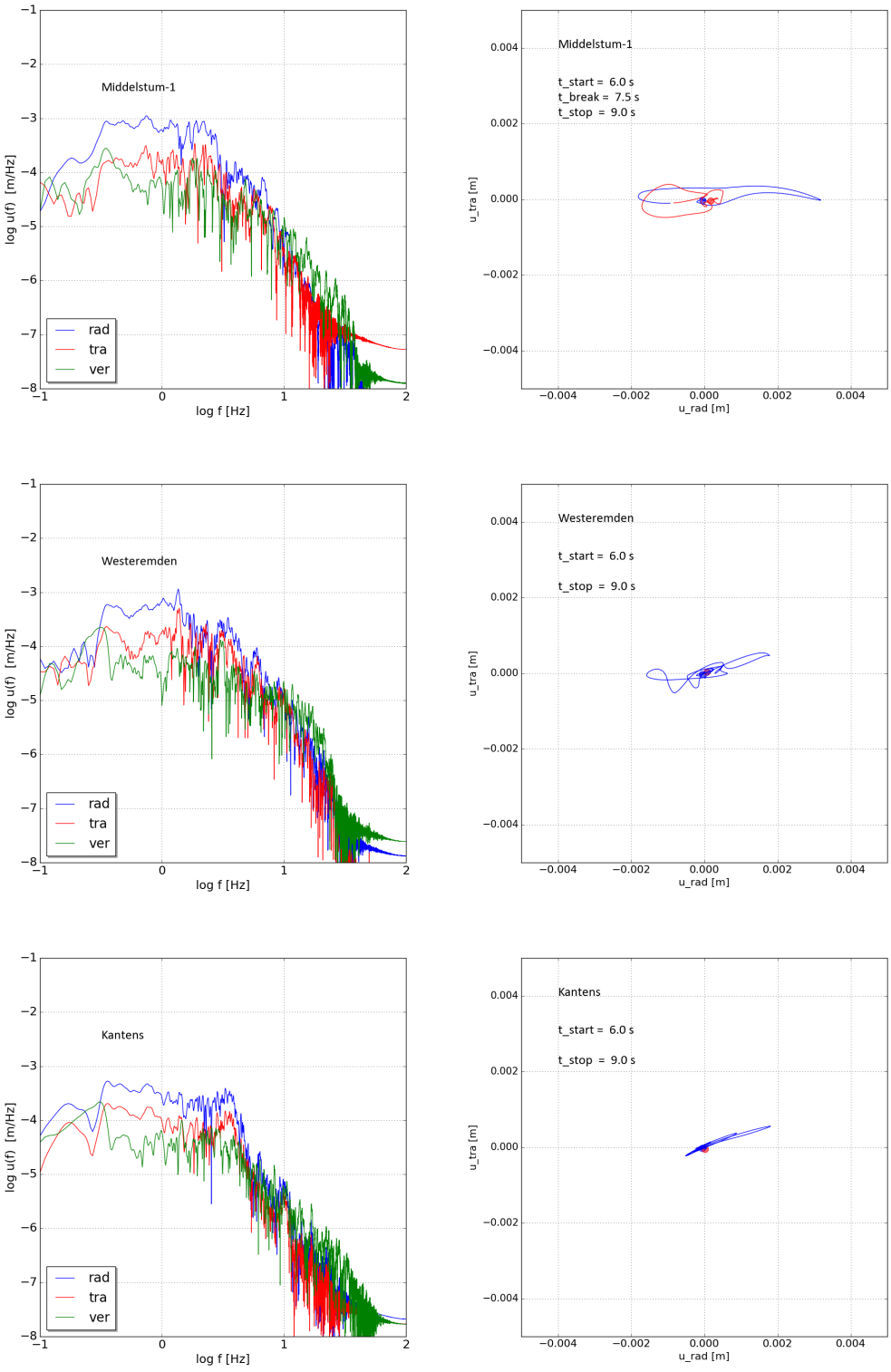

Figure A.2 : Absolute values of Fourier transforms of the displacements (left) and horizontal particle motions over time (right) following from the Huizinge tremor for the Middelstum-1, Westeremden and Kantens accelerometers (from top to bottom).
The blue, red and green solid curves show the Fourier transforms and particle motions of the radial, transverse and vertical displacement components, respectively. The plotted particle motions start at t_{start} (blue dot) and stop at t_{stop} (red dot). This period covers about the passage of the S wave. For the Middelstum-1 accelerometer, the blue and red lines divide the periods in which the first peak and the second peak of the S wave are observed.

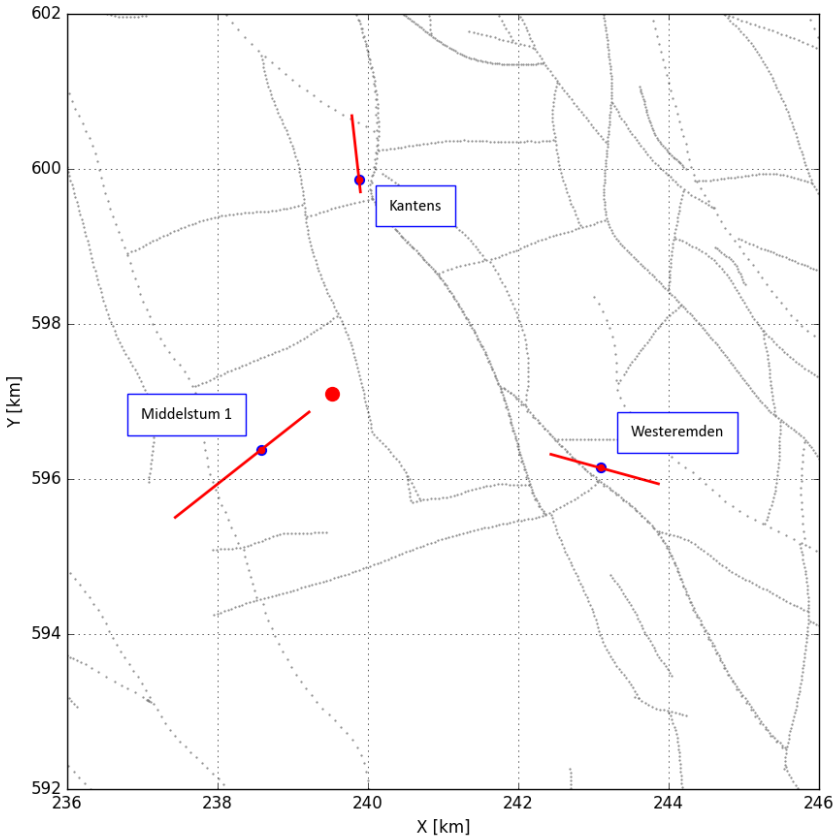

Figure A.3 : Main direction of the accelerometer or particle motions in the horizontal plane following from the Huizinge tremor according to the present accelerometer orientations in the horizontal plane.
The red dot shows the Huizinge tremor epicentre. The blue dots show the accelerometer locations. The red lines, starting from the accelerometer locations, represent the magnitude and main orientation of the accelerometer motions following from the Huizinge tremor. The thin grey dotted and solid lines show the mapped faults.

Appendix B

Additional FEM simulation results

Appendix B.1 Fourier transforms and effect of high-pass filters

Figure B.1 shows the effect of high-pass filters applied to the simulated displacements. To mimic the processing of the accelerometer signals that lead to the observed displacements, the accelerations have been filtered with a 0.1 Hz first order high-pass filter. After integrating the accelerations, the displacements have been filtered with a 0.3 Hz first order high-pass filter. The figure shows that the filters largely reduce the relatively slow and gradual changes in the displacements, as expected.

The effect of the high-pass filter is also visible in Figure B.2 . This figure compares the observed and simulated Fourier transforms of the displacements recorded by the Middelstum-1, Westeremden and Kantens accelerometers. For frequencies below 0.3 Hz, the amplitudes of the spectra decay for lower frequencies. For the non-filtered signals, the spectra would have been flat in this frequency range.

The high-frequency asymptotes of the calculated spectra decay as f^{-n} with n varying in the range 2 - 3 for all accelerometers and displacement components. Differences between the ratios between the amplitudes of observed and calculated spectra correspond with similar differences in the ratios in the amplitudes of the displacements as a function of time. They indicate that the focal sphere may differ from the one proposed and used for the simulations.

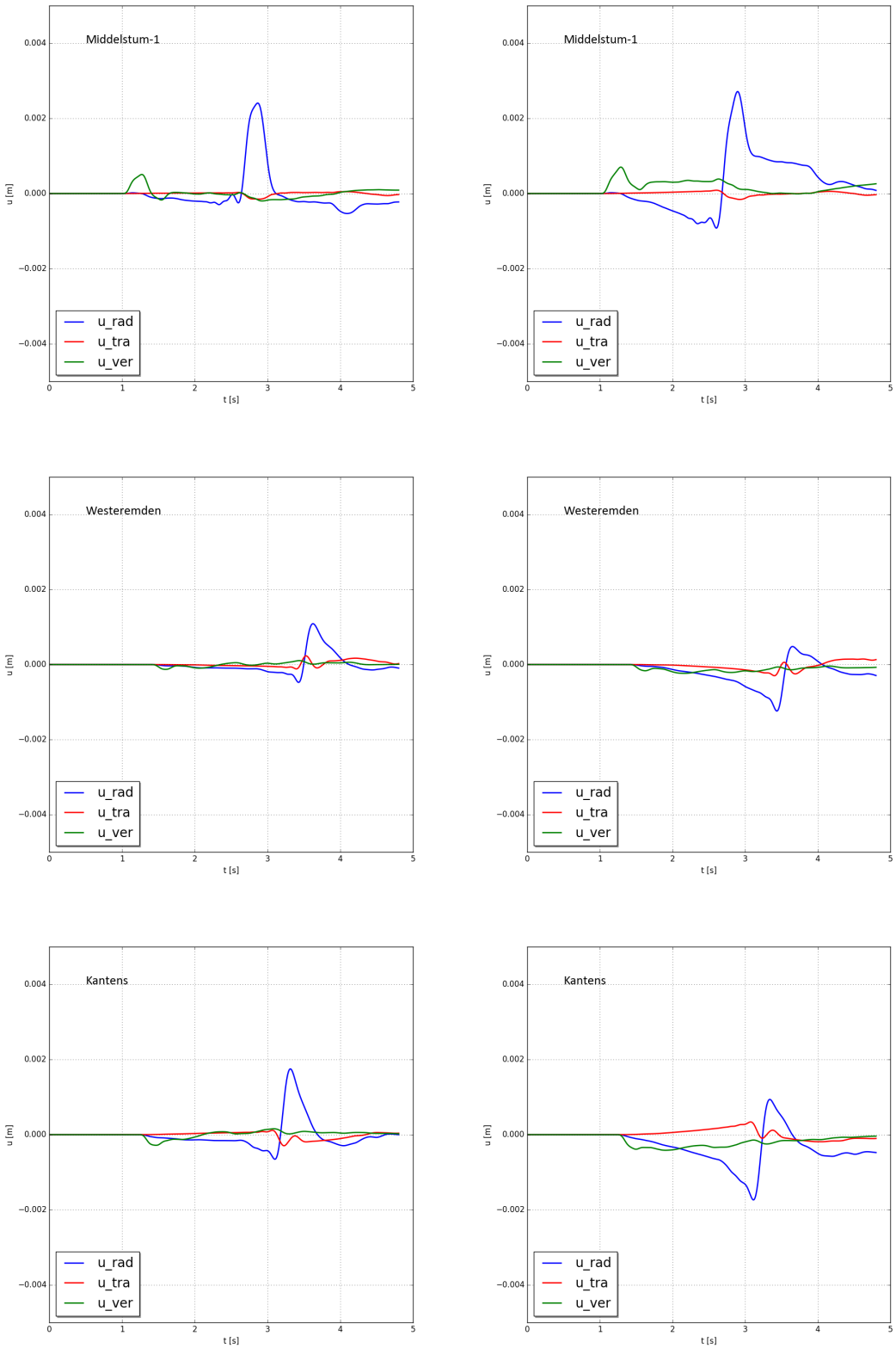

Figure B.1 : Simulated filtered displacements (left) and unfiltered displacements (right) of the Middelstum-1, Westeremden and Kantens accelerometers (from top to bottom) following from the Huizinge tremor.
The blue, red and green curves show the radial, transverse and vertical displacements u_{rad}, u_{tra} and u_{ver}, respectively.

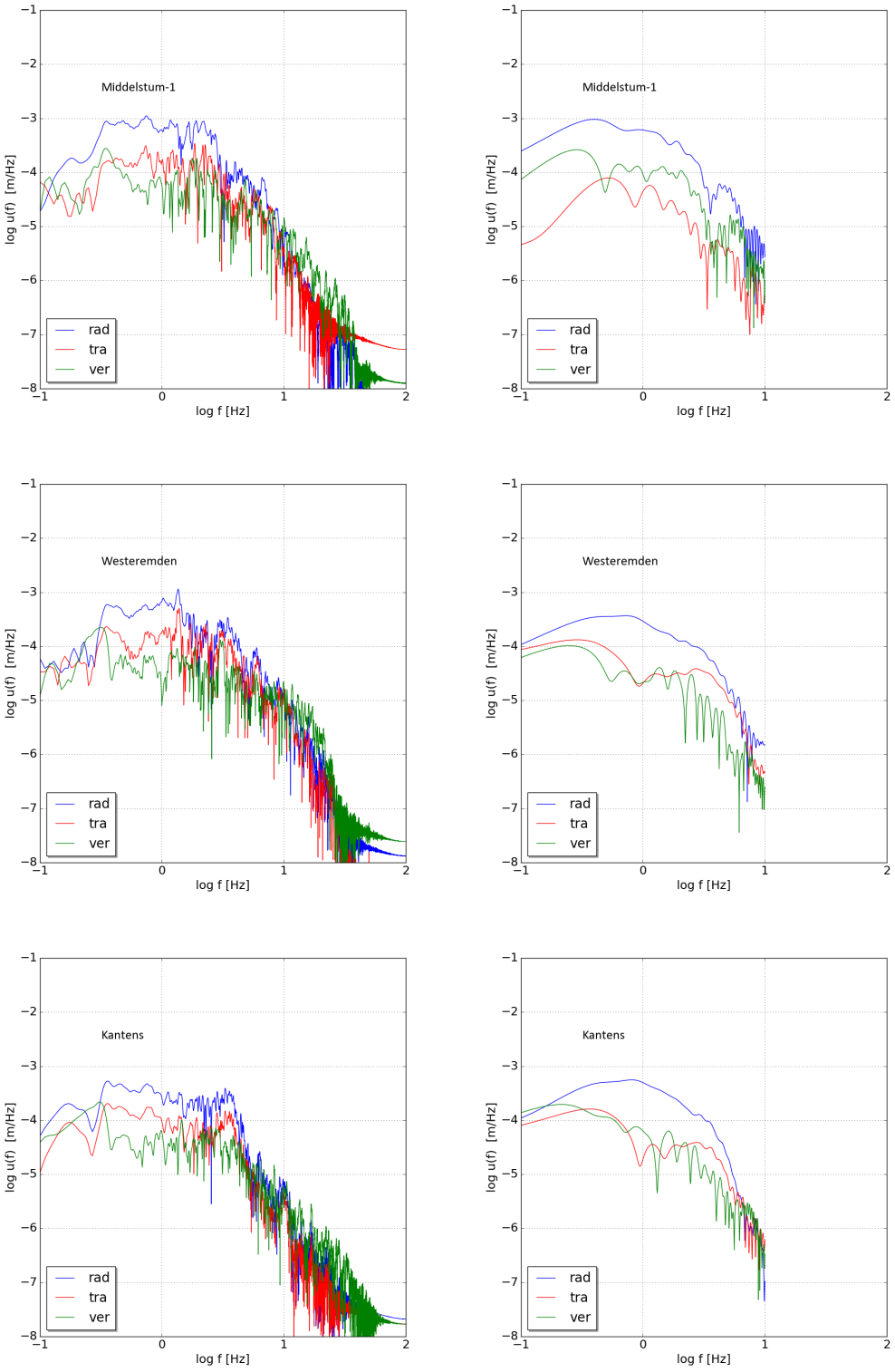

Figure B.2 : Absolute values of Fourier transforms of the observed displacements (left) and simulated displacements (right) for the Middelstum-1, Westeremden and Kantens accelerometers (from top to bottom) following from the Huizinge tremor.
The blue, red and green curves show the Fourier transforms of the radial, transverse and vertical displacements u_{rad}, u_{tra} and u_{ver}, respectively.

Appendix B.2 Source parameter variations

To illustrate the importance of including extended sources in kinematic models for non-uniform overburdens, we show the result of a comparable simulation but for a point source. Also, we show results for a few other fault strike azimuth, fault dip and rake angles.

In all cases the source centre is at 3 km depth. The seismic moment is $M_0 = 300$ TJ. The calculated amplitudes have been multiplied with a factor 2 to include the amplification of the ground motions by the slow down of the waves in the shallow subsurface.

For Figure B.3 the source centre is located at the original Huizinge epicentre. The fault strike azimuth, fault dip and rake angles are $\phi = 160°$, $\delta = 80°$ and λ = -90°, respectively. The Rayleigh damping parameters are $\alpha_{dM} = 0.1$ s $^{-1}$ and $\beta_{dM} = 0$ s for the North Sea formations (corresponding with $Q \sim 40$ for 2 Hz waves) and $\alpha_{dM} = 0.1$ s $^{-1}$ and $\beta_{dM} = 0$ s for the other formations (corresponding with $Q \sim 120$ for 2 Hz waves).

For Figures B.4 - B.6 the source centre is located at the preferred Huizinge epicentre. The fault strike azimuth and fault dip angles are $\phi = 320°$ and $\delta = 80°$, respectively. The rake angle varies. The Rayleigh damping parameters are $\alpha_{dM} = 0.16$ s $^{-1}$ and β_{dM} = 0.00058 s for the North Sea formations and $\alpha_{dM} = 0.08$ s $^{-1}$ and $\beta_{dM} = 0.0029$ s for the other formations. With these damping parameters, the quality factor Q is over a reasonable frequency range constant, i.e. $Q \sim 50$ for the North Sea formations and $Q \sim$ 100 for the other formations, see Appendix C, §C.4.

The following has been varied:

- The source is an extended source or a point source, see Figure B.3 .
- The fault dip is 80° or 65°, see Figures B.4 .
- The rake angle is -90°, 0° or -120°, see Figures B.5 and B.6 .

Figure B.3 shows that the peaks in the displacements from the extended source are more pronounced than for a point source. The signs and relative magnitudes of the three components of the displacements, when compared to each other, do not differ much for both sources[1].

Figure B.4 shows the effect of varying the fault dip angle between 80° and 65° for a fault azimuth and rake angles $\phi = 320°$ and λ = -90°, respectively. Pending on the accelerometer location, the difference in the ratio between the radial and transverse components of the S wave can be larger or smaller. It illustrates that the derivation of the

[1]The high frequency oscillations in the displacements in the left figures are numerical artifacts due to the coarse mesh used. We expect that fast full wave form codes running on parallel computers, using a point source and a finer mesh, can be quite successful in determining the fault azimuth, fault dip and rake angles.

source mechanism from the ground motions should preferably be done using several accelerometers.

Figures B.5 and B.6 show the effect of the rake angle on the displacements. An extreme variation of the rake angle, i.e. between -90° and 0° has a strong effect on all ground motions. In particular, the relative contributions of the transverse and radial components change significantly. On the other hand, a variation between -90° and -120° has a moderate effect on these displacements. To be more certain about the slip direction, the accelerometer orientations in the horizontal plane are important.

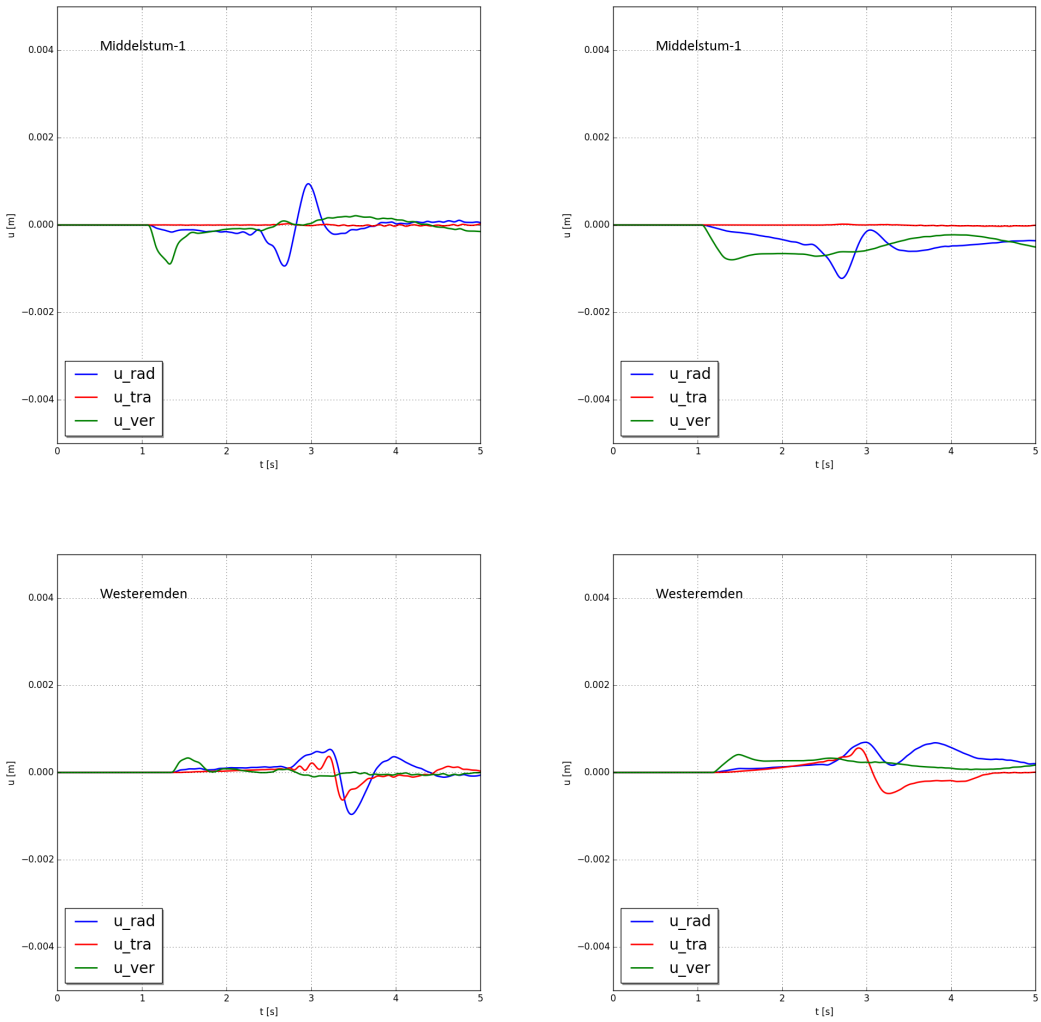

Figure B.3 : Simulated displacements of the Middelstum-1 and Westeremden accelerometers following from the Huizinge tremor with the epicentre at the original location. Ground motions from an extended source (left) and from a similar equi-dimensional source represented by a 'point' source (right).
The fault azimuth, fault dip and rake angles are ϕ = 160°, δ = 80° and λ = -90°, respectively.
The extended source has a length of 0.96 km length along fault strike. The equi-dimensional source is represented by a 'point' source of 0.2 km length along fault strike. The double couple arm of both sources is l_{DC} = 80 m. The source time function parameters for the extended source and the point source are t_{onset} = 5 ms, t_r = 0.08 s and n = 2 and t_{onset} = 5 ms, t_r = 0.2 s and n = 2, respectively. The rupture velocity $V_{r,strike}$ along fault strike is 2 km/s.
The blue, red and green curves show the radial, transverse and vertical displacements u_{rad}, u_{tra} and u_{ver}, respectively.

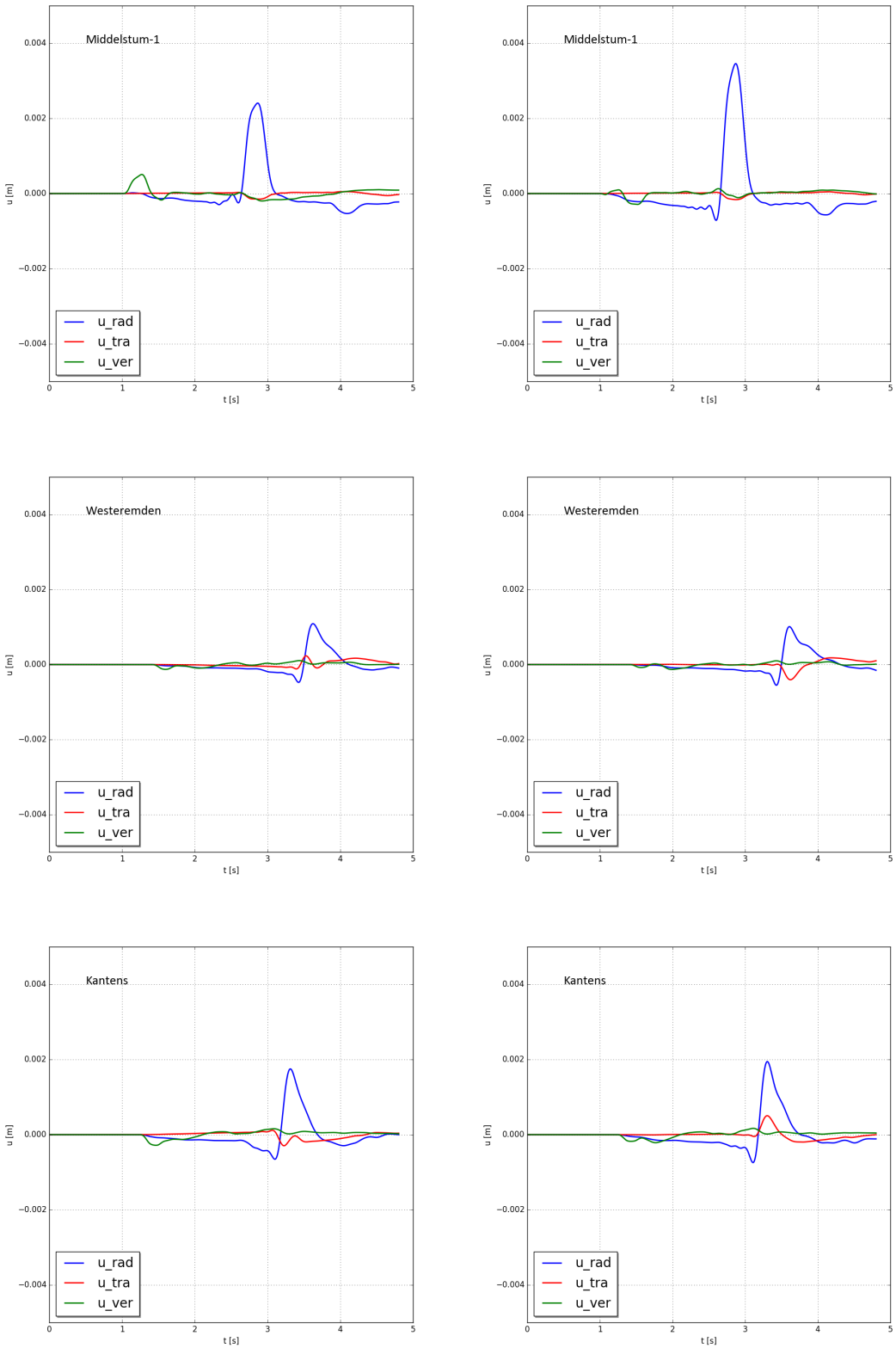

Figure B.4 : Simulated displacements of the Middelstum-1, Westeremden and Kantens accelerometers (from top to bottom) following from the Huizinge tremor. Ground motions from two extended sources with fault dips $\delta = 80°$ (left) and $\delta = 65°$ (right). For both sources, the fault azimuth and rake angles are $\phi = 320°$ and λ = -90°, respectively. The radial, transverse and vertical displacements, u_{rad}, u_{tra} and u_{ver} are shown by the blue, red and green curves, respectively.

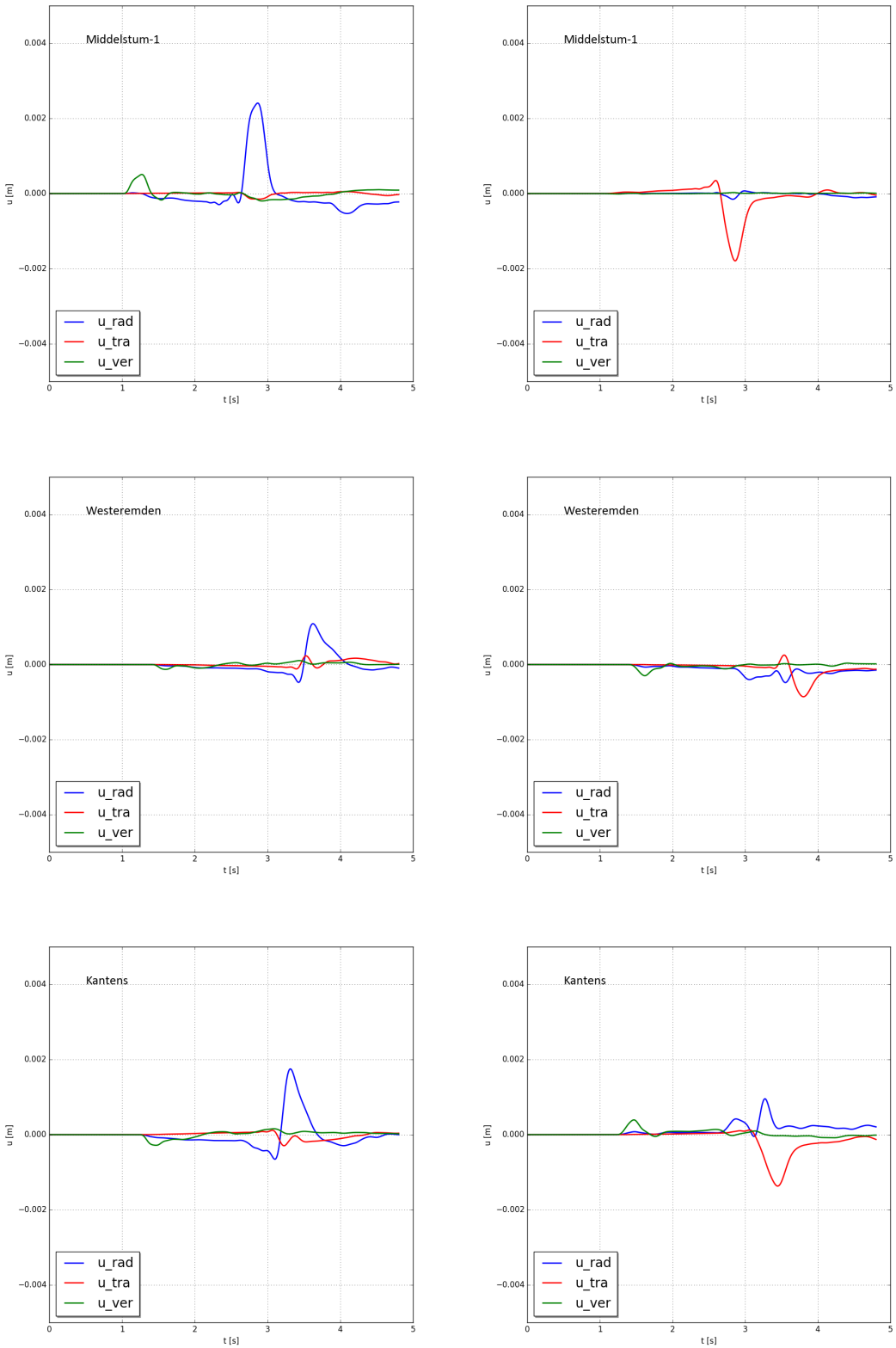

Figure B.5 : Simulated displacements of the Middelstum-1, Westeremden and Kantens accelerometers (from top to bottom) following from the Huizinge tremor. Ground motions from two extended sources with rake angles λ = -90° (left) and $\lambda = 0°$ (right). For both sources, the fault strike azimuth and fault dip angles are $\phi = 320°$ and $\delta = 80°$, respectively. The blue, red and green curves show the radial, transverse and vertical displacements u_{rad}, u_{tra} and u_{ver}, respectively.

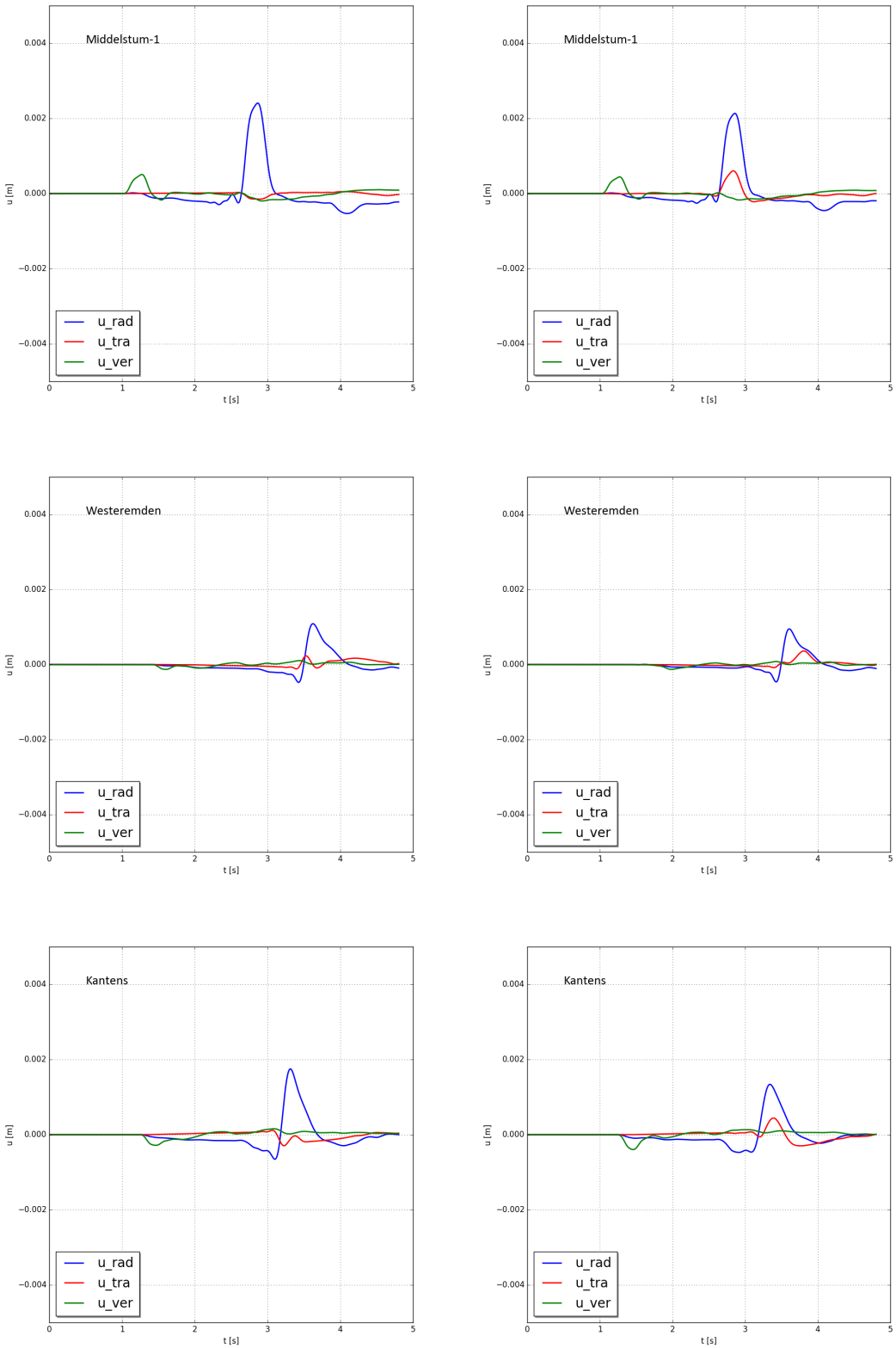

Figure B.6 : Simulated displacements of the Middelstum-1, Westeremden and Kantens accelerometers (from top to bottom) following from the Huizinge tremor. Ground motions from two extended sources with rake angles λ = -90° (left) and λ = -120° (right). For both sources, the fault strike azimuth and fault dip angles are ϕ = 320° and δ = 80°, respectively.
The blue, red and green curves show the radial, transverse and vertical displacements u_{rad}, u_{tra} and u_{ver}, respectively.

Appendix B.3 Body waves reaching the surface

Figures B.7 - B.10 show the effect of the slip direction on the ground motions near the epicentre. The figures are snapshots of the ground displacements when the P and S waves pass or are close to the three accelerometers of interest. The first rupture has a slip direction vertically downwards along fault dip, i.e. with a rake angle λ = -90°. The second one has a slip direction along fault strike, i.e. with a rake angle λ = 0°. The first one could follow from stress release induced by gas production. The second one could follow from stress release caused by non-isotropic horizontal field stresses resulting from old tectonic motions.

The sources are at 3 km depth and located at the preferred Huizinge epicentre and have a seismic moment M_0 = 300 TJ. The fault strike azimuth, fault dip and rake angles are ϕ = 320°, δ = 80°, respectively. The Rayleigh damping parameters are $\alpha_{dM} = 0.16$ s $^{-1}$ and $\beta_{dM} = 0.00058$ s for the North Sea formations and $\alpha_{dM} = 0.08$ s $^{-1}$ and $\beta_{dM} = 0.0029$ s for the other formations.

Displacement directions substantially vary along the fault plane and result in complicated horizontal vector patterns. Height variations in the subsurface landscape in the overburden have a minor effect on the low frequency content of the waves.
For slip along fault dip with a rake angle λ = -90°, the wave fronts of the vertical and radial components are about symmetrical with respect to a line perpendicular to fault strike. The wave front of the transverse component is about anti-symmetrical with respect to the same line. The vectors show that at 3.2 s after the start of the rupture, when the S-wave pass the three accelerometers, the horizontal displacements recorded by these accelerometers is predominantly radial.
For slip along fault strike with rake angle λ = 0°, the sign of the vertical and radial components change every 90 degrees rotating over the source receiver azimuth angle ϕ'. The wave front of the transverse component is symmetrical with respect to a line parallel to fault strike. The S wave leads to a strong oscillation in transverse direction along this line.
Assuming that the accelerometer orientations are correct, the observed strong positive radial displacements of both the Westeremden and Kantens accelerometers would not be easily explained by a source with a slip predominantly along fault strike along this fault plane or along the other fault plane identified by EBN. The sign of the radial component varies to quickly with the source receiver azimuth angle.

The depth variations in the horizon between the Zechstein formation and the Trias formation have a minor effect on these symmetries. A small effect is seen for the wave fronts of the vertical component of the extended source with a slip along fault strike.

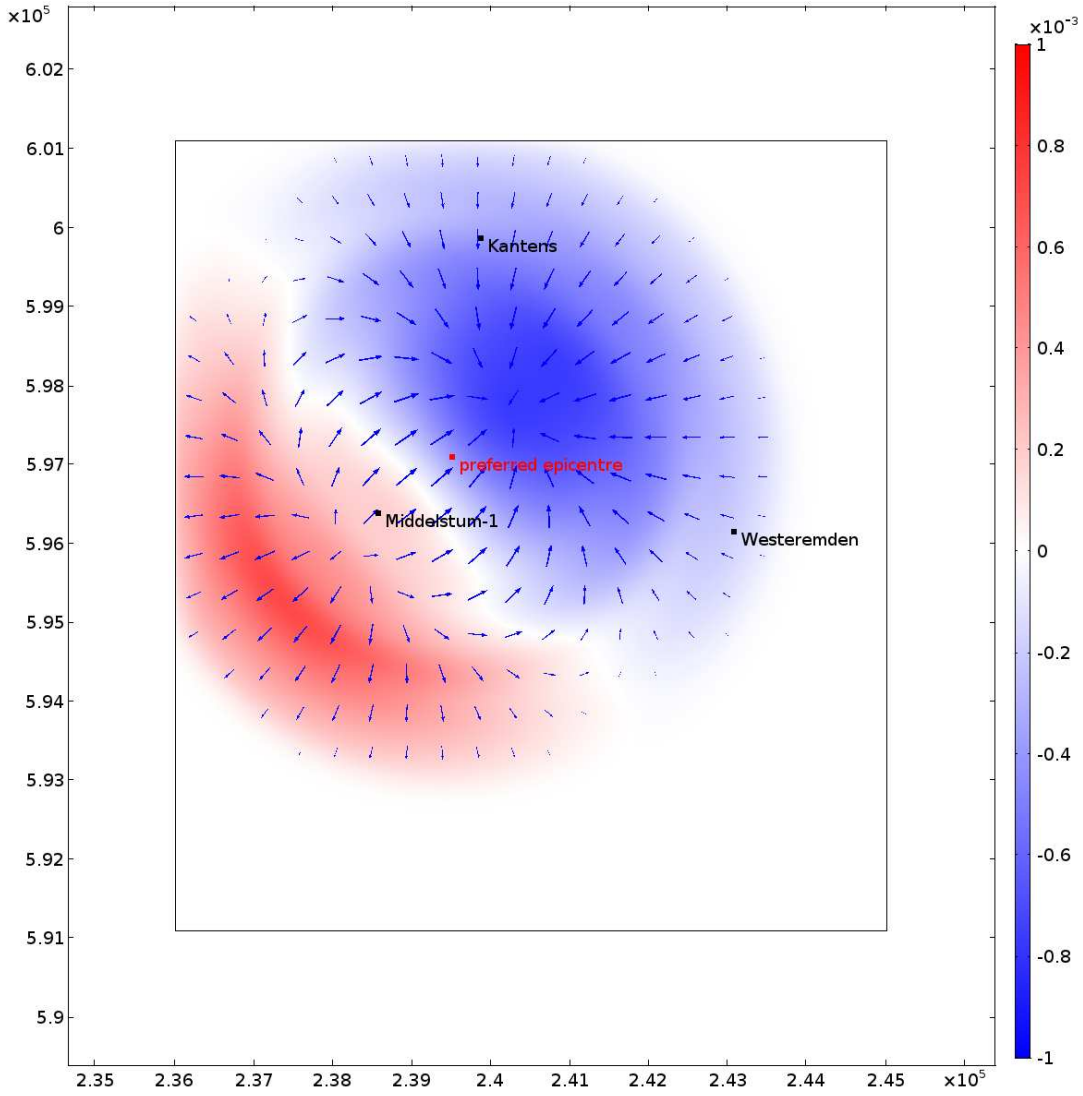

Figure B.7 : Snapshot of vertical displacements u_{ver} at the surface at 1.6 s after the start of the rupture for an extended source with rake angle λ = -90°.
The blue vectors show the direction and logarithmic magnitude of the horizontal displacements. The red and black dots show the tremor epicentre and accelerometer locations.

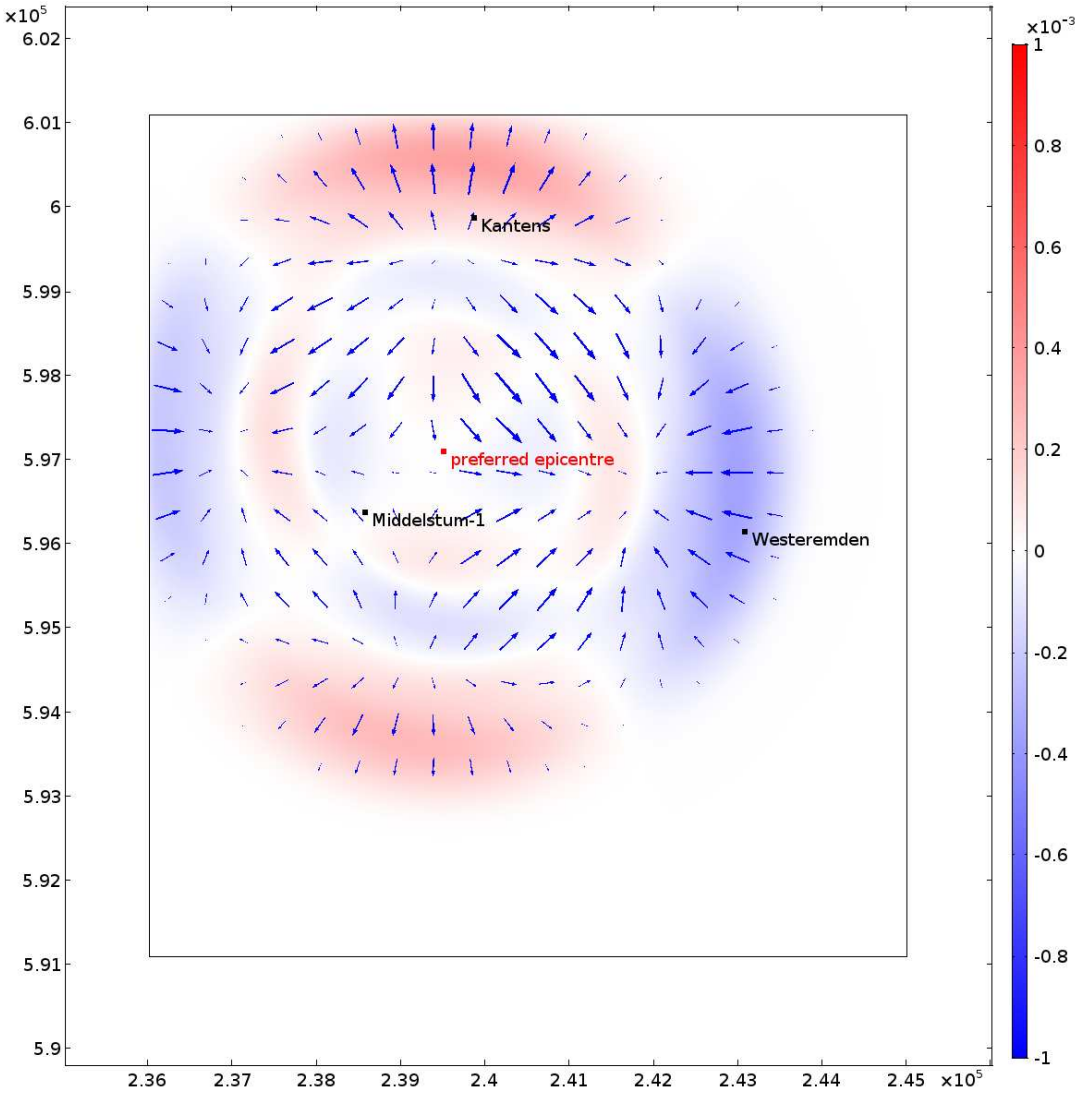

Figure B.8 : Snapshot of vertical displacements u_{ver} at the surface at 1.6 s after the start of the rupture for an extended source with rake angle $\lambda = 0°$.
The blue vectors show the direction and logarithmic magnitude of the horizontal displacements. The red and black dots show the tremor epicentre and accelerometer locations.

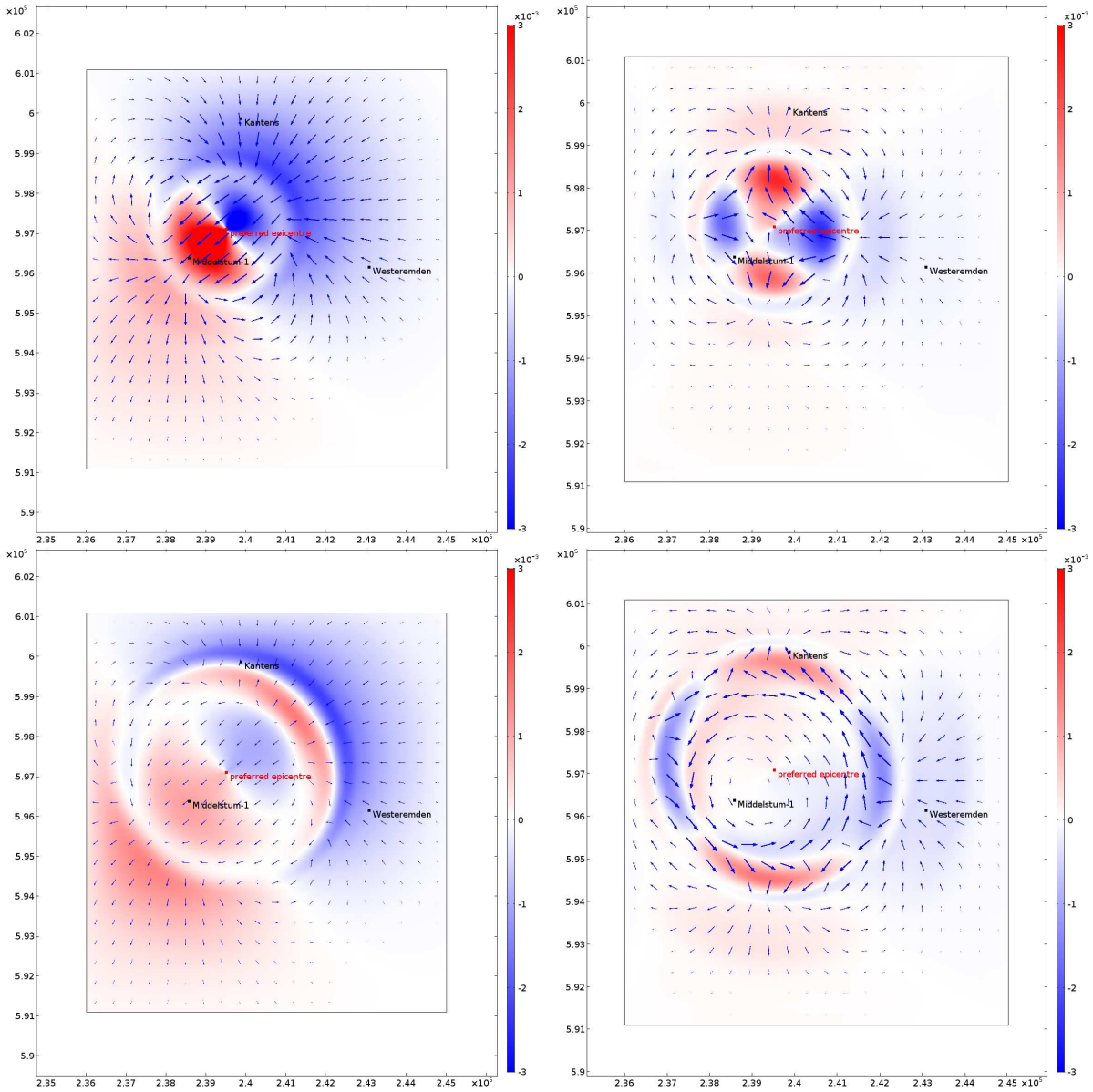

Figure B.9 : Snapshot of radial displacements u_{rad} at the surface at 2.8 s (top) and 3.2 s (bottom) after the start of the rupture for extended sources with rake angles λ = -90° (left) and $\lambda = 0°$ (right), respectively.
The blue vectors show the direction and logarithmic magnitude of the horizontal displacements. The red and black dots show the tremor epicentre and accelerometer locations. The left figures for rake angle 0° can be directly compared with the unfiltered displacements shown in Figure B.1 . The red coloured sickle in the left bottom figure in the direction of the Kantens and Westeremden accelerometers corresponds with the positive radial displacement peaks recorded by these accelerometers.

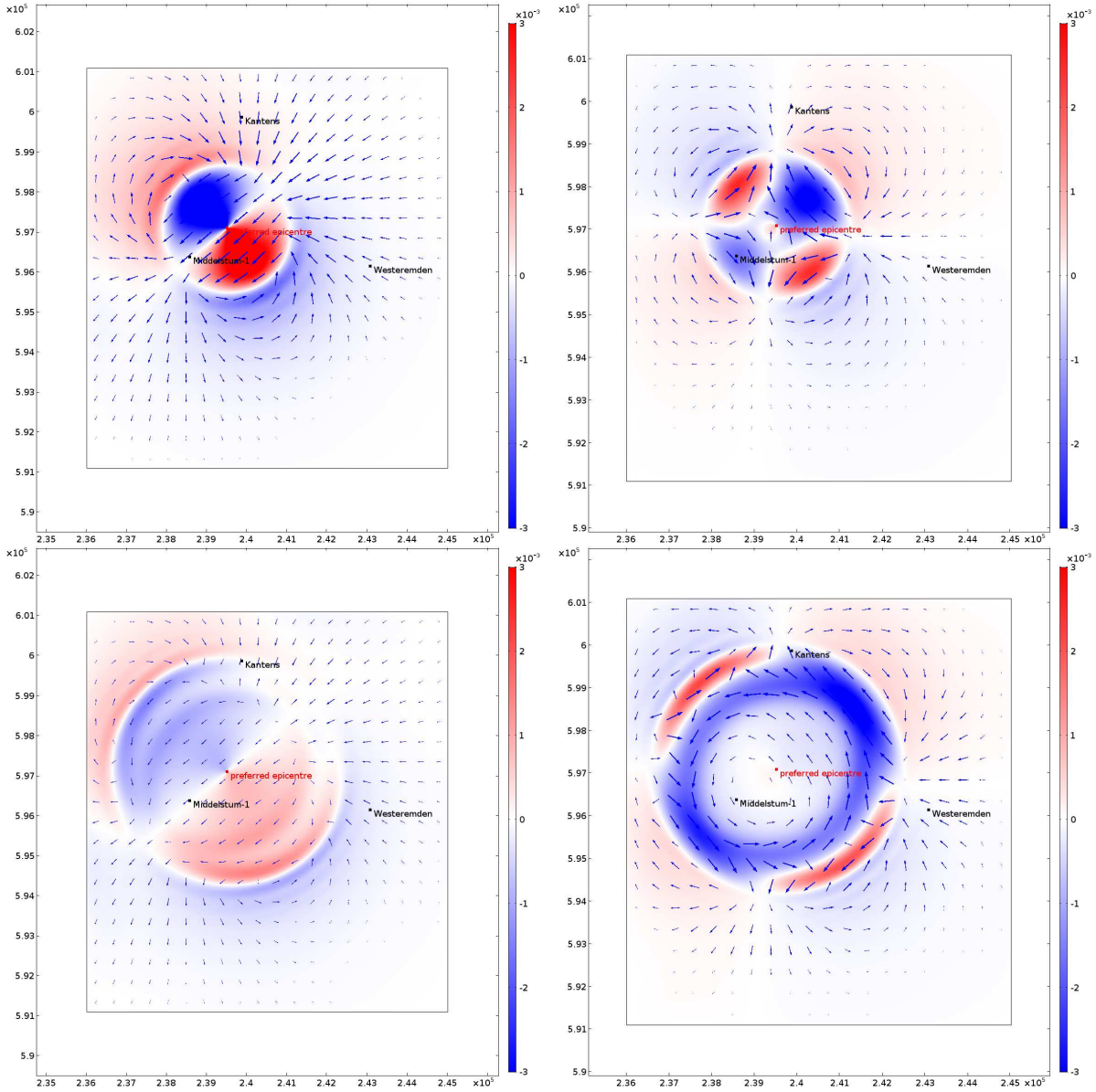

Figure B.10 : Snapshot of transverse displacements u_{tra} at the surface at 2.8 s (top) and 3.2 s (bottom) after the start of the rupture for extended sources with rake angles λ = -90° (left) and $\lambda = 0°$ (right), respectively.
The blue vectors show the direction and logarithmic magnitude of the horizontal displacements. The red and black dots show the tremor epicentre and accelerometer locations.

Appendix C

Finite element method simulations

Appendix C.1 Source

C.1.1 Fault orientation and slip direction

The definitions of the coordinate system, parameters for the fault plane orientation and slip direction follow from Aki and Richards (2009), §4.5, Figure C.1 . Note that the (x,y) coordinates used differ from the (X,Y) Dutch Rijksdriehoeksstelsel coordinates. The positive x-axis is to the north and the positive y-axis is to the east while the positive X-axis is to the east and the positive Y-axis is to the north. We distinguish these two coordinate systems by small and capital letters.
The fault orientation is specified by the fault azimuth and fault dip angles, ϕ and δ [degree/radian]. The relative displacement or slip D [m] is in the direction of the motion of the hanging wall relative to the foot wall. The slip direction is defined by the rake angle λ [degree/radian] which is the angle between the strike and slip directions. For $\lambda = 0$, the slip is parallel to fault strike. Equivalently, the fault orientation and slip direction are defined by the unit vectors $\boldsymbol{n}$ and $\boldsymbol{l}$, respectively.

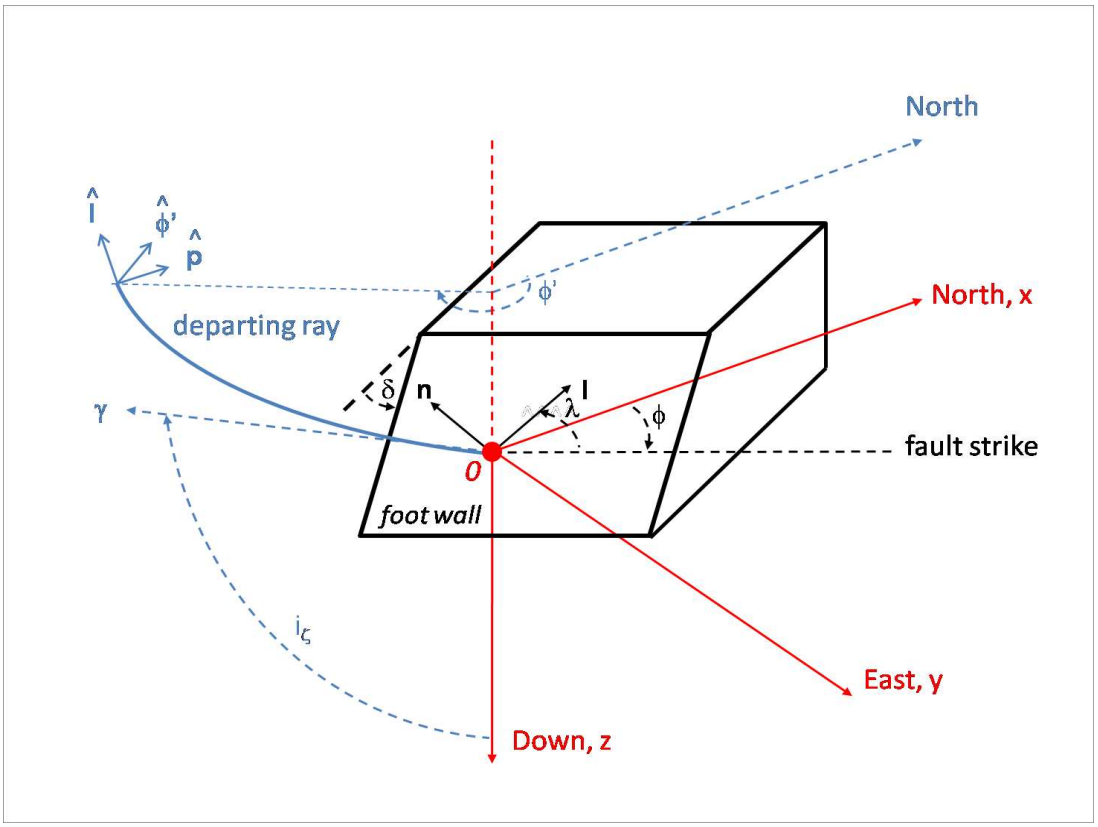

Figure C.1 : Right-handed (x,y,z) or (north,east,down) Cartesian coordinate system (red axis), fault geometry and parameters for rupture or fault plane and slip direction. The positive part of the z-axis is pointing downwards. The fault plane has two surfaces, i.e. the hanging wall and the foot wall (black lines). The surface shown is from the foot wall. The origin is at the tremor epicentre, i.e. the point of the Earth's surface vertically above the centre of this seismic source which result from slip on a normal fault.
The strike direction of the fault is the one of the two horizontal directions in the fault plane for which the block containing the hanging wall is on the right as viewed by an observer looking along strike. The fault strike azimuth angle ϕ is the angle between the Earth north direction and the fault strike where it is measured clockwise round from north. The fault dip angle δ is measured down from the horizontal plane.
The slip refers to the motion of the hanging wall relative to the foot wall. The slip direction is defined by the rake angle λ which is the angle between the strike direction (horizontal dashed line in the fault plane) and the slip direction. The rake angle is measured in the fault plane and has a negative value when directed downwards with respect to the horizontal. So, λ = -90° for normal faulting when the hanging wall would slide down compared to the foot wall.
$\boldsymbol{l}$ [-] is the slip-direction unit vector and $\boldsymbol{n}$ [-] is the unit vector normal to the foot wall and pointing towards the hanging wall.
The blue line shows the geometrical ray of the departing body wave of interest. $\hat{\boldsymbol{l}}$, $\hat{\boldsymbol{p}}$ and $\hat{\boldsymbol{\phi}}'$ are the unit vectors in the direction of the departing ray at the receiver location. i_ζ is the take-off angle of the body wave ray through the receiver. ϕ' is the azimuth angle of the receiver with respect to the north direction seen from the source epicentre which is in the origin of the (x,y,z) coordinate system. For a homogeneous medium, $\boldsymbol{l} = \boldsymbol{\gamma}$.

C.1.2 Double couples

Forces causing a shear displacement along a small plane can be represented by four point forces around the centre of this plane. These point forces form a so-called double couple, see for example Udias et al. (2014), §4.2. This seismic source is defined by the location, orientation and magnitude of these point forces.
To represent a point source, the arm of the double couple l_{DC} should be considerably smaller than the length scales of the domain considered and the source-receiver distance. Further, l_{DC} should be smaller than $\sim 1/4$ wavelength for the frequency range of interest. For an upper limit of 5 Hz, and a rupture velocity of $V_r = 0.8V_s \sim 2$ km/s, the wavelength is $\lambda = V_r/f \sim 0.4$ km. So, $l_{DC} \leq 100$ m should be sufficient.

Double couple for slip along fault dip

For the modelling of a rupture with slip along fault dip in the simulations, we have used another set of four point forces, equivalent to two double couples, see the right figure in Figure C.2 . For this configuration,

$$f(t) = \frac{M_0}{2l_{DC}} f_{stf}(t), \tag{C.1.1}$$

where M_0 is the seismic moment of the source.

For an extended rupture along fault strike and with the slip direction along fault dip, we have used four line forces through the locations of the point forces of the double couples and with a force per meter length equal to $f'(t) = f(t)/L$ where L is the length of the rupture plane along fault strike. The line forces are along the blue lines at the edges of a grey plane in Figure C.3 . For a rake angle of -90°, the slip direction of the hanging wall is downwards.

Double couple for slip along fault strike

For an extended rupture along fault strike and with the slip direction along fault strike, we have used a series of double couples in a plane along fault strike and perpendicular to the fault plane, see the red dots for the locations of the point forces in Figure C.3 . The arm length of these double couples is equal to the arm length of the double couple line forces used for the slip along fault dip.

Double couple for slip in any direction

For slip along the fault plane with rake angle λ, the contribution of the slip component along fault dip is multiplied by a factor $\sin|\lambda|$ and the contribution of the slip component along strike is multiplied by a factor $\cos\lambda$.

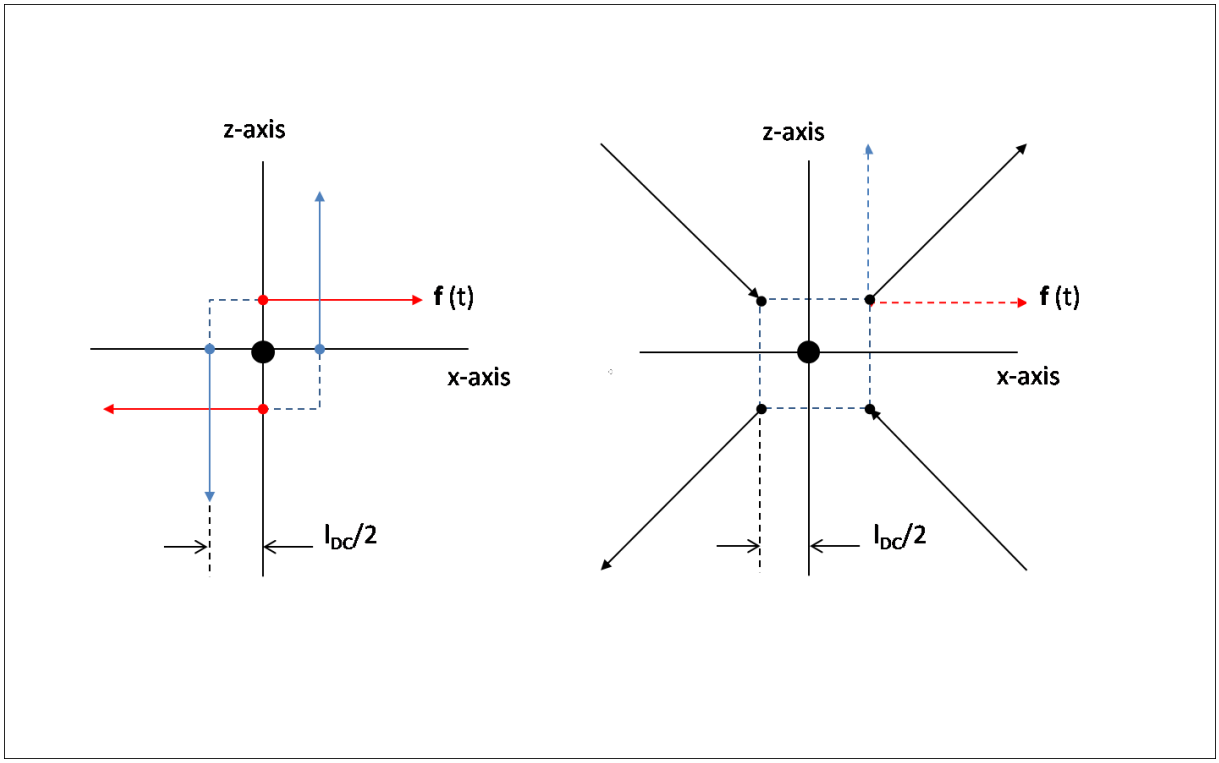

Figure C.2 : Two equivalent sets of point forces to construct a double couple around the centre of a seismic point source (black dot in origin). The left one shows a convenient double couple, see for example Udias et al. (2014), Figure 4.1. The two couples are represented by the horizontal couple of forces (red arrows) and the vertical couple of forces (blue arrows) of equal strength $f(t)$ [N].
The distance between the point forces of each couple is the 'arm' of the double couple l_{DC} [m], equal to the size of the rectangle shown. This set of forces generates a relative displacement along a fault plane along the z-axis. The left plane is moving downwards and the right one is moving upwards.
For FEM simulations, we represent the seismic point source by an equivalent set of point forces as shown in the right figure. The origins of the force vectors are on the corners of the same rectangle and point in the direction of the black arrows. Each vector is the sum of a horizontal force vector (dashed red) and a vertical force vector (dashed blue) of the same strength as those in the left figure.
Both sets of forces are equivalent to a moment tensor. The equivalent seismic moment of the double couple is for the set of point forces in the left figure $M_0(t) = l_{DC} f(t)$ and for the set of point forces in the right figure $M_0(t) = 2l_{DC} f(t)$, see also Udias et al. (2014), Eq. 4.7.

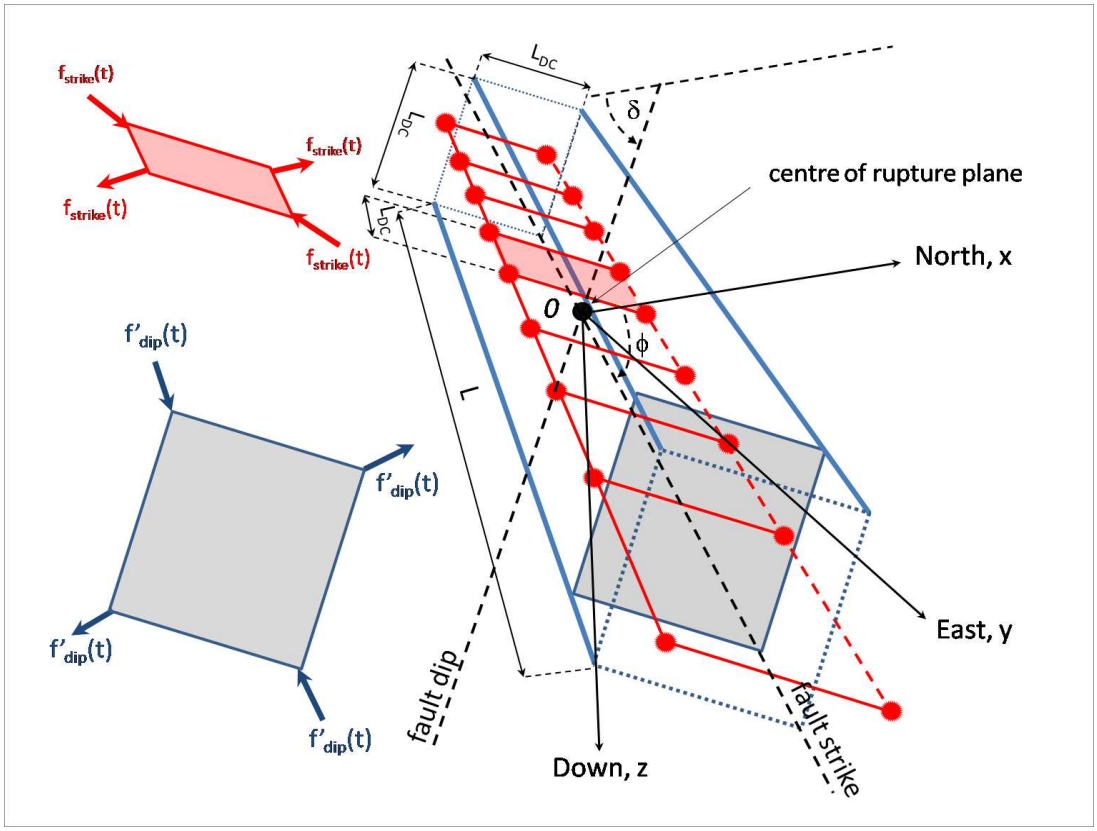

Figure C.3 : Two sets of double couples for an extended rupture along fault strike with length L. The blue set is for slip along fault dip, the red one for slip along fault strike. The black lines show the coordinate system and the fault strike and fault dip. The centre of the source or rupture plane is at the origin O.
The blue lines are the locations of the four line forces for slip along fault dip. The line forces lie in the grey coloured face shown. The force directions are indicated by the blue arrows in the same grey face at the bottom left side of the figure.
The red dots are the locations of the point forces for slip along fault strike. Each set of four dots form a double couple lying in the red plane. In this example, a series of 8 double couples with arm lengths l_{DC} are distributed at equal distances over the rupture plane along fault strike, such that $L = 8l_{DC}$. All dots, except those at the two ends of the rupture plane, are locations for point forces of two adjacent double couples.

Appendix C.2 Subsurface geometry

The subsurface formations are modelled by analytical expressions for the horizons based on three dimensional point clouds, using an application tool provided by Comsol^{TM}. These expressions approximate reasonably well the horizons derived from seismic data and which are given in the form of depth values on a fine 25×25 m grid.

Figures C.4 - C.7 show horizons between a few formations and their analytical proxys used in the model. The horizons have a size of 10×10 km and are centred around the coordinates $X = 240$ km and $Y = 595$ km, which is close to the epicentre of the Huizinge tremor. The proxys are based on so-called point clouds defined on a 30×30 grid with square grid cells of 333×333 m. The depth values in each grid cell grid are local averages. The analytical proxys are smoother than the NAM horizons, especially near faults with large throws, such as in the south-west part of the region of interest. For the low frequencies and long wavelengths of interest, these deviations have no major effect on the calculated displacements.

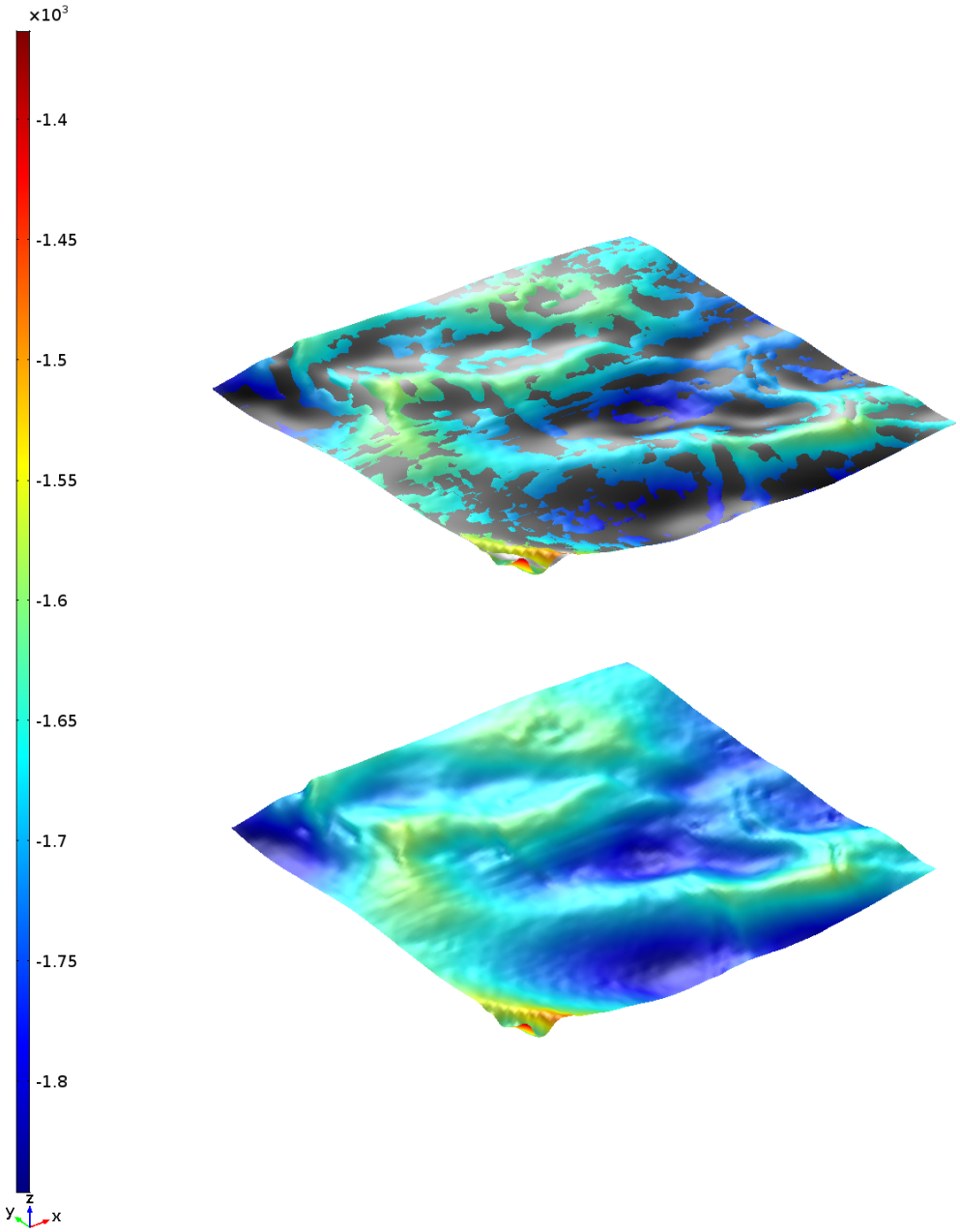

Figure C.4 : Proxy for the horizon between the Rijnland and Chalk formations. The lower plane is the horizon according to NAM data. The upper plane shows again this horizon but also a gray coloured horizon which is the analytical proxy. Sometimes, the analytical horizon is above the NAM horizon and the colour gray appears, sometimes it is below the NAM horizon and the colour of the latter horizon appears. This horizon at a mean depth of 1.8 km is in the model the upper horizon of the lumped Trias, Altena and Rijnland formation.

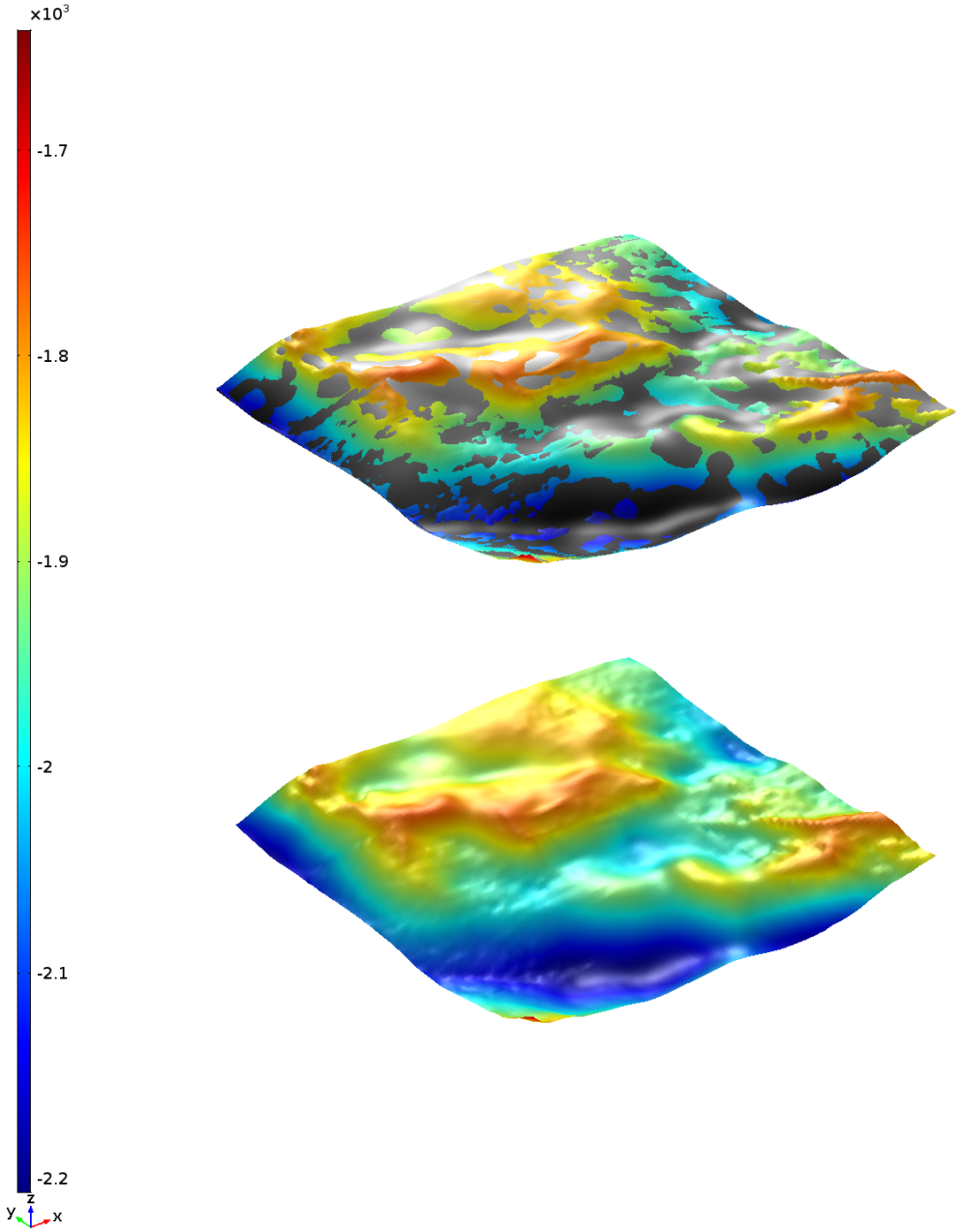

Figure C.5 : Proxy for the horizon between the upper Zechstein and the Trias formation, see for an explanation Figure C.4 . The substantial slopes in this horizon at a mean depth of 1.9 km follow from salt tectonism.

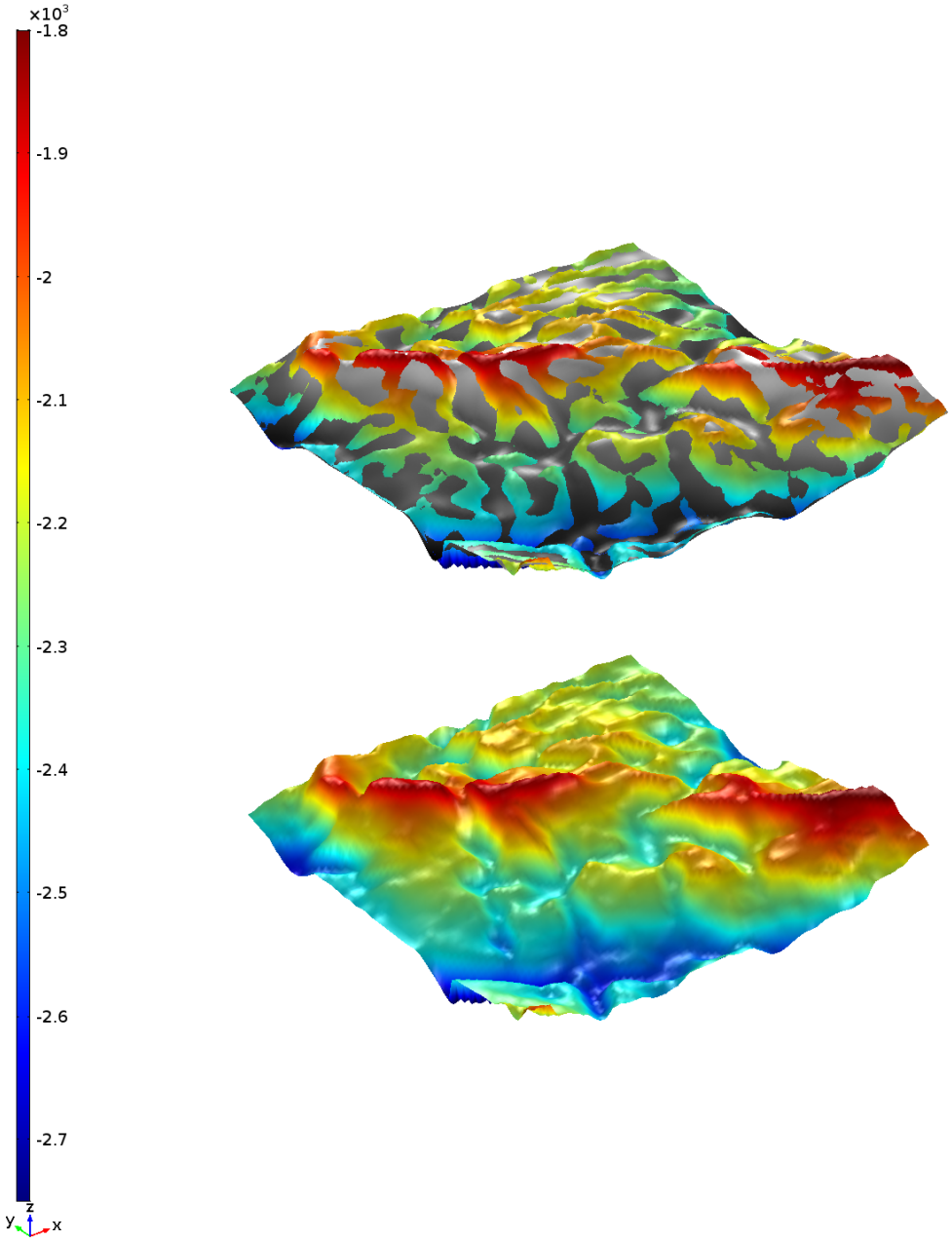

Figure C.6 : Proxy for the horizon between the lower Zechstein and the floater, see for an explanation Figure C.4 . The substantial slopes in this horizon at a mean depth of 2.2 km follow from salt tectonism.

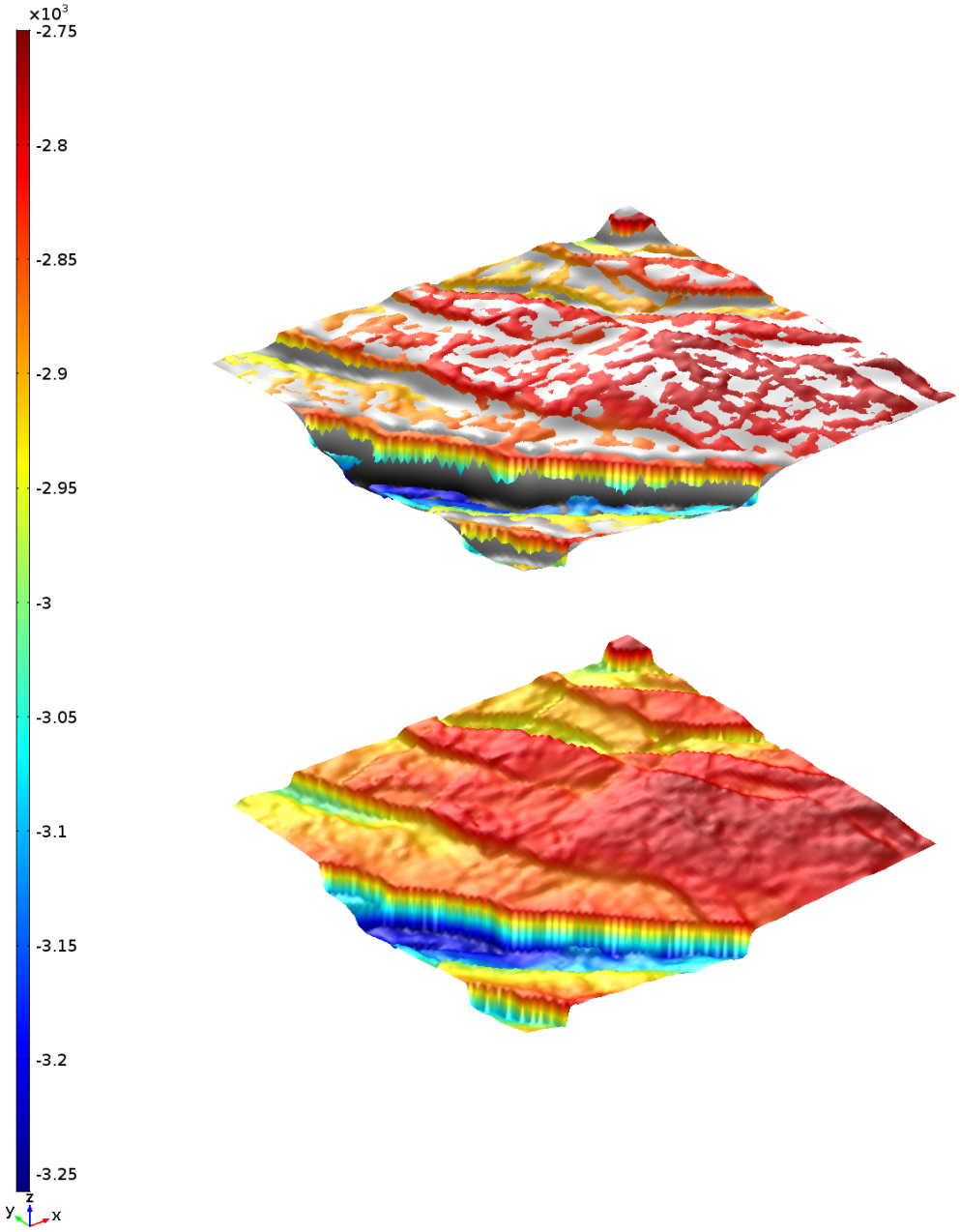

Figure C.7 : Proxy for the horizon between the reservoir and the overlaying anhydrite, see for an explanation Figure C.4 .
The horizon at a mean depth of 2.9 km clearly shows prints of many faults in various directions. The horizon between the anhydrite and the lower Zechstein is about 50 m above this horizon and nearly parallel to it.

Appendix C.3 Velocity model

The subsurface wave velocities V_p and V_s depend on the subsurface formation and on the depth according to the following equations

$$V_p(z) = V_{p,0} + k_p|z| \quad \text{and} \quad V_s(z) = V_{s,0} + k_s|z|. \tag{C.3.1}$$

$V_{p,0}$ and $V_{s,0}$ [m/s] are the P and S wave velocities for $z = 0$. k_p and k_s [1/s] are constants which determine the dependence of the wave velocities on depth. For the various formations, these velocity input parameters are given in §C.2, Table C.1 .

In the region around Huizinge, the Altena formation is practically absent and the Rijnland formation is relatively thin. To simplify the geometry, these formations have been lumped to one formation. Disregarding the Altena formation in the region around Huizinge, we have used the following expressions for the P and S wave velocities

$$V_p(z) = f(z)\big(V_{p,0,tri} + k_{p,tri}|z|\big) + (1 - f(z))\big(V_{p,0,rnl} + k_{p,rnl}|z|\big),$$

and

$$V_s(z) = f(z)\big(V_{s,0,tri} + k_{s,tri}|z|\big) + (1 - f(z))\big(V_{s,0,rnl} + k_{s,rnl}|z|\big). \tag{C.3.2}$$

$f(z)$ is a smooth step function $f(z) = 1$ for $z <$ -1.75 km and $f(z) = 0$ for $z >$ -1.75 km[1]. The subscripts 'tri' and 'rnl' stand for the Trias and Rijnland formations, respectively.

$$V_s(z) = f(z)\big(V_{s,0,tri} + k_{s,tri}|z|\big) + (1 - f(z))\big(V_{s,0,rnl} + k_{s,rnl}|z|\big), \tag{C.3.3}$$

Lumping the floater and upper Zechstein formation into one upper Zechstein formation, the velocity profile in this lumped formation is given by

$$V_p(z) = V_{p,0,uz} + \frac{V_{p,0,fl} - V_{p,0,uz}}{1 + \exp(0.05(z - 60 - z_{lz,fl}(x, y))},$$

and

$$V_s(z) = V_{s,0,uz} + \frac{V_{s,0,fl} - V_{s,0,uz}}{1 + \exp(0.05(z - 60 - z_{lz,fl}(x, y))}. \tag{C.3.4}$$

The subscripts 'uz', 'lz' and 'fl' stand for the upper Zechstein and lower Zechstein formations and the floater, respectively. $z_{lz,fl}$ [m] is a function which describes the lower horizon of the floater. These expressions imply that the wave velocities in the first 60 m above the lower Zechstein-floater horizon are equal to those in the floater.

[1]The size of the transition zone of the step function in Comsol^{TM} is 50 m.

Lumping the anhydrite layer and lower Zechstein formation into one lower Zechstein formation, the velocity profile in this lumped formation is given by

$$V_p(z) = V_{p,0,lz} + \frac{V_{p,0,an} - V_{p,0,an}}{1 + \exp(0.05(z - 60 - z_{rs,an}(x,y))},$$

and

$$V_s(z) = V_{s,0,lz} + \frac{V_{s,0,an} - V_{s,0,lz}}{1 + \exp(0.05(z - 60 - z_{rs,an}(x,y))}. \qquad \text{(C.3.5)}$$

The subscripts 'rs' and 'an' stand for the reservoir and anhydrite formations, respectively. $z_{rs,an}$ [m] is a function which describes the lower horizon of the anhydrite formation. These expressions imply that the wave velocities in the first 60 m above the reservoir-anhydrite horizon are equal to those in the anhydrite.

We have not modelled the poorly mapped thin Brussels sand formation at about 500 m depth. This formation leads to a shallow reflector for waves of frequencies higher than a few Hz. The Ten Boer claystone, which forms the upper part of the reservoir, is included in the reservoir formation. The shallow sand, clay and peat layers in the Upper North Sea formation have not been modelled in these simulations.

Table C.1 : Input parameters for the velocity model 2015 of NAM for the various formations.

Formation name used	$V_{p,0}$ m/s	k_p 1/s	$V_{s,0}$ m/s	k_s 1/s
Upper North Sea	1733	0.500	458	0.430
Lower North Sea	1922	0.500	614	0.430
Chalk	680	2.300	-5	1.390
Rijnland	2125	0.500	701	0.420
Altena	2222	0.355	1364	0.190
Trias	2383	0.680	1450	0.380
upper Zechstein	4300	0	2436	0
floater	5729	0	3152	0
lower Zechstein	4475	0	2524	0
anhydrite	6000	0	3288	0
Rotliegend reservoir	3800	0	2232	0
Carboniferous underburden	2572	0.541	837	0.500

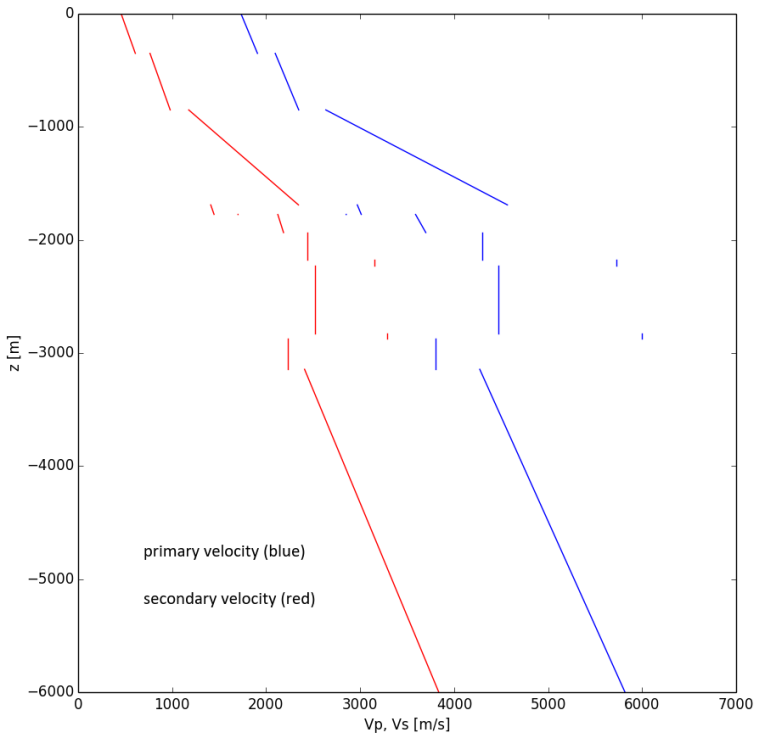

Figure C.8 : P and S wave velocities versus depth profiles in the region around the Huizinge tremor epicentre, according to the NAM 2015 velocity model. The velocity profiles are based on the mean depths of the horizons in this region, given in Appendix A, Table A.2 .

Appendix C.4 Wave damping in the subsurface

In the simulations, waves are damped by activating Rayleigh damping. The Rayleigh damping terms are included in the elasto-dynamic equations as

$$\rho\frac{\partial^2 \boldsymbol{u}}{\partial t^2} + \alpha_{dM}\rho\frac{\partial \boldsymbol{u}}{\partial t} - \nabla\cdot(\boldsymbol{S} + \beta_{dM}\frac{\partial \boldsymbol{S}}{\partial t}) = 0. \qquad \text{(C.4.1)}$$

Herein is $\boldsymbol{S}$ [Pa] is the stress tensor. The Rayleigh damping coefficients α_{dM} [1/s] and β_{dM} [s] relate to the damping factor D (or the so-called isotropic loss factor ζ) [-] as

[2]

$$D = \frac{1}{2}\Big(\frac{\alpha_{dM}}{\omega'} + \beta_{dM}\omega'\Big). \tag{C.4.2}$$

ω' [radian/s] is the undamped resonance circular frequency of possible standing waves in the system considered. For propagating waves, ω' can be replaced by the dominant frequency of the wave. Rayleigh wave damping is frequency dependent. For non-zero α_{dM} and $\beta_{dM} = 0$, D decreases with increasing frequency.

In most simulations, we have used for the Lower and Upper North Sea formations α_{dM} = 0.16 s $^{-1}$ and β_{dM} = 0.00058 s and α_{dM} = 0.08 s $^{-1}$ and β_{dM} = 0.0029 s for the other formations. With these damping parameters, the quality factor Q is over a reasonable range of frequencies constant, i.e. $Q \sim 50$ for the North Sea formations and $Q \sim 100$ for the other formations. The higher damping in the North Sea formations suppresses the generation of artificial high frequency oscillations in these formations for the element size used. The damping is quite moderate. When the damping would have been the same as in the other formations, the amplitudes would increase well within the uncertainties about wave amplification and damping in the shallow subsurface.

In a few other simulations, we have used for the North Sea formations $\alpha_{dM} = 0.3$ s $^{-1}$ and $\beta_{dM} = 0$ s. For waves with a dominant frequency of 2 Hz, the corresponding damping and quality factors are $D = \alpha_{dM}/(4\pi f) \sim 0.012$ and $Q = 1/(2D) \sim 40$. For the other subsurface formations, we use $\alpha_{dM} = 0.1$ s^{-1} and $\beta_{dM} = 0$ s. For the same 2 Hz waves, the corresponding $D \sim 0.004$ and $Q \sim 120$. The quality factor increases for higher frequencies.

Figure C.9 shows the damping factor D as a function of frequency in the frequency range of interest. A more constant damping factor over a reasonable frequency range can be obtained by using a combination of non-zero parameters α_{dM} and β_{dM}.

The simulations don't include the slow down of the S waves in the upper part of the Upper North Sea formation, i.e. in the shallow subsurface. In the Groningen field, the shallow subsurface contains clay and peat layers. The S wave velocity in these shallow

[2] Take a one-dimensional shear wave with a circular frequency ω' propagating and attenuated in the upward z-direction. The displacement can be expressed as $u(t,z) = A(z)\exp\big[i(\omega' t - kz)\big]$, where the wave number $k = \omega'/\beta$ and $A(z) = A_0\exp(-\eta z)$. The attenuation coefficient η [m^{-1}] relates to the damping factor D [-] as $\eta = \omega' D/\beta$.
Take $\beta_{dM} = 0$. Substituting this into Eq. (C.4.1) and noting that $\nabla \cdot \boldsymbol{S}$ simplifies to $\mu\partial^2 u/\partial z^2$, A_0 is non-zero (or we have a non-trivial solution) if

$$-\omega'^2 + i\alpha_{dM}\omega' - \frac{\mu}{\rho}\big(\eta^2 + 2ik\eta - k^2\big) = 0.$$

This expression can be rewritten for weakly damped waves, using $\beta^2 = \mu/\rho$, $k^2 = \omega'^2/\beta^2$ and$\eta \ll k$, as

$$\alpha_{dM}\omega' - \beta^2 2k\eta \approx 0 \quad or \quad \alpha_{dM} \approx 2\beta\eta = 2\omega' D.$$

sedimentary layers is substantially lower than in the deep formations or the so-called base-rock. In general, V_s increases from peat layers (50 - 100 m/s) to clay layers (80 - 150 m/s) to sand layers (up to 200 m/s for Holocene and higher values for Pleistocene). Further, V_s values scatter over a wide range for a given litho-stratigraphical class and statistical calculation methods are needed to calculate the average effect and possible variations of the effect of the shallow surface on seismic waves.
The quality factor Q in the shallow subsurface is believed to be in the range 10 - 20. Combined with the slow down of the S waves, it leads to an amplification of the amplitudes of the S-waves with a factor of about 2 according to reports about ground motion prediction equations, see e.g. NAM (2015) and the references herein and in line with Dost et al. (2004). For two-dimensional simulations, the FEM simulations yield a similar amplification factor. For three dimensional simulations, we may include these effects in the future pending on available computer power.

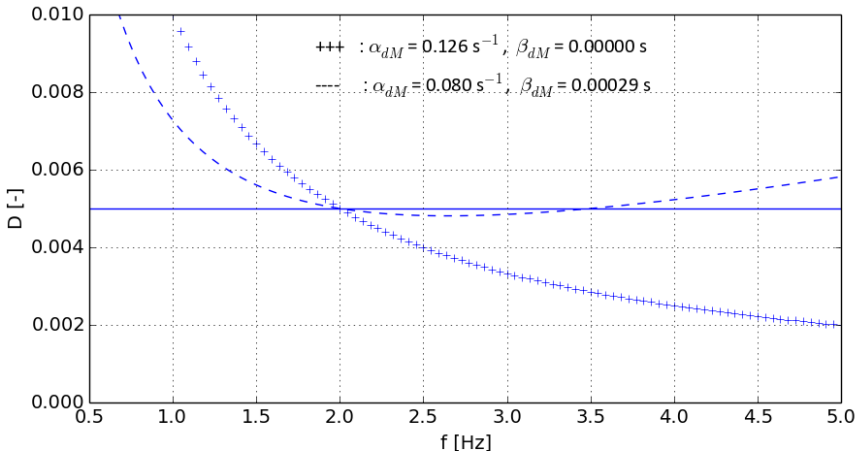

Figure C.9 : Damping factor D as a function of frequency for two sets of Rayleigh damping parameters α_{dM} and β_{dM}. The solid line shows a constant damping factor $D = 0.005$, or quality factor $Q = 100$. Using a combination of non-zero values for α_{dM} and β_{dM} a rather constant damping factor can be obtained over a reasonable frequency range of 1 - 5 Hz (dashed line).
Using $\alpha_{dM} = 0.126$ s^{-1} and $\beta_{dM} = 0$ s (crossed line), 1 Hz waves have a damping factor of $D = 0.01$ and a corresponding $Q = 50$. For 4 Hz waves, $D = 0.0025$ and $Q = 200$.

C.4.1 Solver and mesh

In Comsol^{TM}, we used the time dependent solver based on the so-called Generalized Alpha method and the default GMRES iterative solver with multigrid option and with a mesh coarsening factor of 2 and quadratic discretisation of the displacement field. To obtain a

good compromise between computation time and the accuracy of the calculated waves, we have applied general criteria from textbooks to minimise numerical dispersion of the waves and numerical or artificial oscillations[3]. The three-dimensional uniform domain is 9×10 or 10×10 km wide and 6 km deep. The grid in the overburden has a maximum element size of 80 m. The grid is considerably refined around the source represented by double couple line forces. The grid in the underburden has a maximum element size of 300 m to reduce computational time. Wave propagation in this part of the subsurface is of no interest for this work.
Low reflecting boundaries have been used for the side and bottom boundary planes of the domain. Both P and S waves leave the domain at these planes with little numerical reflection. However, at the interface with the free boundary plane or the surface, the waves are reflected at the edges with the low reflecting boundaries and lead to artificial waves reflected back into the domain.

Figures C.10 and C.11 show simulations for wave propagation in a uniform medium. The fault strike azimuth, fault dip and rake angles are $\phi = 160°$, $\delta = 85°$ and λ = -90°, respectively. So, the footwall of the normal fault is east from the hanging wall. The P and S wave velocities are 3.2 km/s and 1.5 km/s, respectively. These values correspond with mean values of these wave velocities in the overburden. The Rayleigh wave damping parameters are $\alpha_{dM} = 0.3$ s^{-1} and $\beta_{dM} = 0$ s for the North Sea formations and $\alpha_{dM} = 0.1$ s^{-1} and $\beta_{dM} = 0$ s for the other formations.
The extended source, in the form of double couple line forces, is along fault strike over a length of 960 m. The centre of the source is located at 3 km depth at the original epicentre of the Huizinge tremor which deviates somewhat from the preferred one. The arm of the double couple line force source is $l_{DC} = 80$ m.
The source time function used is the modified source time function Eq. (3.1.5) with shape parameters $t_r = 0.08$ s, $n = 2$. The rupture starts at the centre of the source on the z-axis and propagates with a rupture velocity $V_{r,strike} = 2$ km/s in both directions along fault strike. The source has a seismic moment of $M_0 \sim 300$ TJ with a corresponding magnitude $M = 3.55$[4].

Simulations for a non-uniform domain require a maximum element size of 50 m in the North Sea formations because of the low shear velocity in these formations. It leads to a

[3]A rule of thumb for the maximum size of the elements or grid cells follows from the maximum wave frequency of interest f_{max} and the lowest wave velocity, i.e. the shear velocity, V_s. For an accurate wave model, using quadratic discretisation of the space, about 6 grid cells are required in one wavelength. For $f_{max} = 3$ Hz and for a mean shear velocity of $V_s = 1.5$ km/s, $\lambda \sim 500$ m and element size should be about $\Delta s \sim 80$ m where s stands for x, y, z.
To minimise the wave dispersion when waves propagate through the thin anhydrite layer above the reservoir or through the thin floater in the Zechstein, we use smaller time steps than would follow from the general Courant condition, $\delta t \sim \Delta s / V_s$.

[4]The equivalent magnitude of the line forces per unit length f' which representing the seismic source in the FEM simulation follows from the relation $f' = M_0/(2 l_{DC} L)$ [N/m] where l_{DC} is the arm of the double couple and L is the length of the fault plane in strike direction, see §C.1.

model with about 18 million elements and about 80 million degrees of freedom (DOF). It takes about 50 hours for 5 s simulation, using a time step 2 ms and 48 cores in parallel operating on 512 GB shared memory.

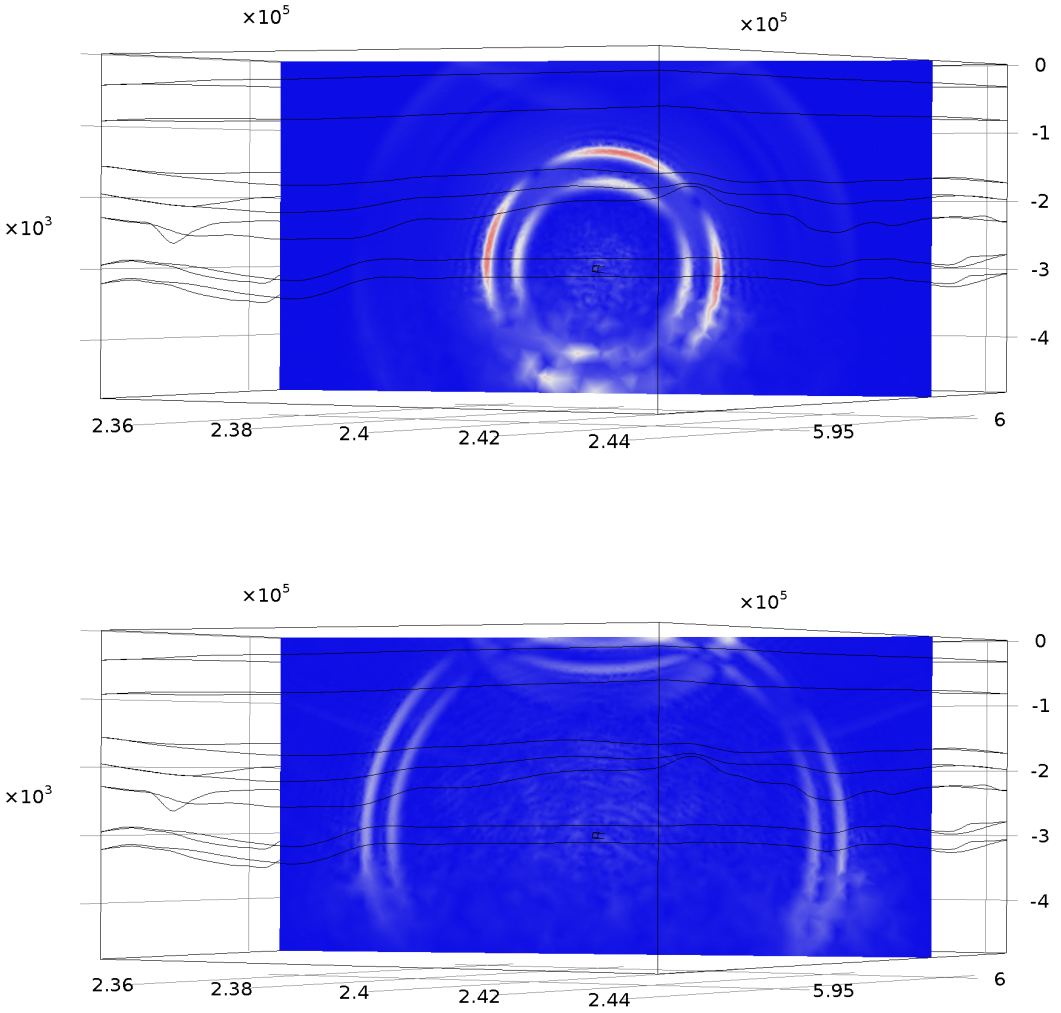

Figure C.10 : Propagation of waves from a tremor in a three-dimensional 10×10×6 km uniform domain using a maximum element size of 80 m. The source and conditions are described in the text. The top and bottom figures show two snapshots of the total displacement velocity at 1.2 s and 2.4 s in a plane with the same orientation as the plane for the two dimensional simulations. The P and S wave velocities in the domain are uniform and are 3.2 km/s and 1.5 km/s, respectively.
The wave is poorly resolved in the underburden because of a larger maximum element size of 300 m in this part of the domain.

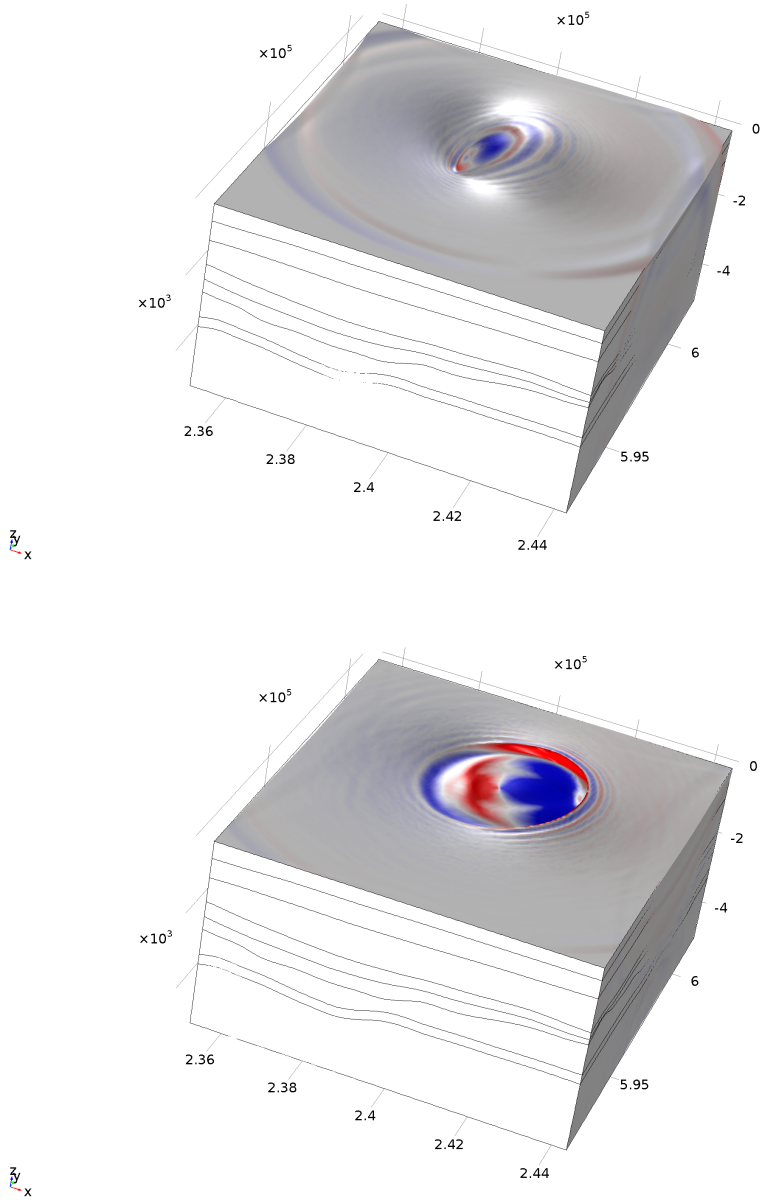

Figure C.11 : Propagation of a tremor in a three-dimensional 10×10×6 km uniform domain using a maximum element size of 80 m. The source and conditions are described in the text and are similar as those used in Figure C.10 .
The figures show three-dimensional snapshots of the ground deformation at 2.0 s (top) and 2.4 s (bottom). The colours refer to the radial velocity. The black curved lines along the side walls of the domain show the intersections of the horizons of the formations with the side walls.
The colours show the radial displacement velocity: red is positive, blue is negative. The red and blue fringes upfront of the S wave correspond with the small artificial 10 Hz oscillations in Figure C.12 which occur before the arrival of the S wave.

C.4.2 Comparison with analytical solutions

Figure C.12 shows the radial and vertical displacement velocities of the Middelstum-1 accelerometer from simulations and from analytical solutions for an extended source along fault strike. The extended source for the simulation, in the form of double couple line forces, is along fault strike over a length of 960 m. The centre of the source is located at 3 km depth at the original epicentre of the Huizinge tremor which deviates somewhat from the preferred one. The arm of the double couple line force source is $l_{DC} = 80$ m. The extended source for the analytical calculations, in the form of a series of 21 moment tensors, is along fault strike over the same length. The sources have a seismic moment of $M_0 \sim 300$ TJ.

The analytical solutions originate from moment tensor solutions for wave propagation in uniform isotropic elastic infinite media, see Aki and Richards (2009), §4.3, Eq. 4.29.

The fault strike azimuth, fault dip and rake angle are in this case $\phi = 160°$, $\delta = 85°$ and λ = -90°, respectively. The P and S wave velocities are 3.2 km/s and 1.5 km/s, respectively. The amplitudes of the displacements of the analytical solution have been multiplied by a factor 2 to account for the doubling of the wave amplitudes at the free surface.

The source time function for the generated wave is the modified source time function Eq. (3.1.5) with shape parameters $t_r = 0.08$ s, $n = 2$. The rupture starts at the centre of the source on the z-axis and propagates with a rupture velocity $V_{r,strike} = 2$ km/s in north and south directions along fault strike.

Figure C.13 shows the corresponding displacements which follow from integrating the displacement velocities over time. Although absolute values somewhat differ, the main shape of the curves is quite well reproduced by the simulations[5]. Apart from high frequency oscillations, this also holds for the small transverse displacements. For larger source accelerometer distances the correspondence between analytical solutions and simulations deteriorates.
This figure also shows the results (dashed lines) of simulations for damped waves using Rayleigh damping. Somewhat stronger 10 Hz oscillations appear because in this case the maximum element size in the overburden is 100 m. The Rayleigh damping parameters are $\alpha_{dM} = 0.3$ s^{-1} and $\beta_{dM} = 0$ s for the North Sea formations and $\alpha_{dM} = 0.1$ s^{-1} and $\beta_{dM} = 0$ s for the other formations. Damping reduces the displacement amplitudes by about 20%.

[5]The displacements amplitudes are two times smaller than those for a source with the same seismic moment shown in the main text and in Appendix B because the wave amplification ny a factor 2 due to wave slow down in the shallow subsurface is not included in this example.

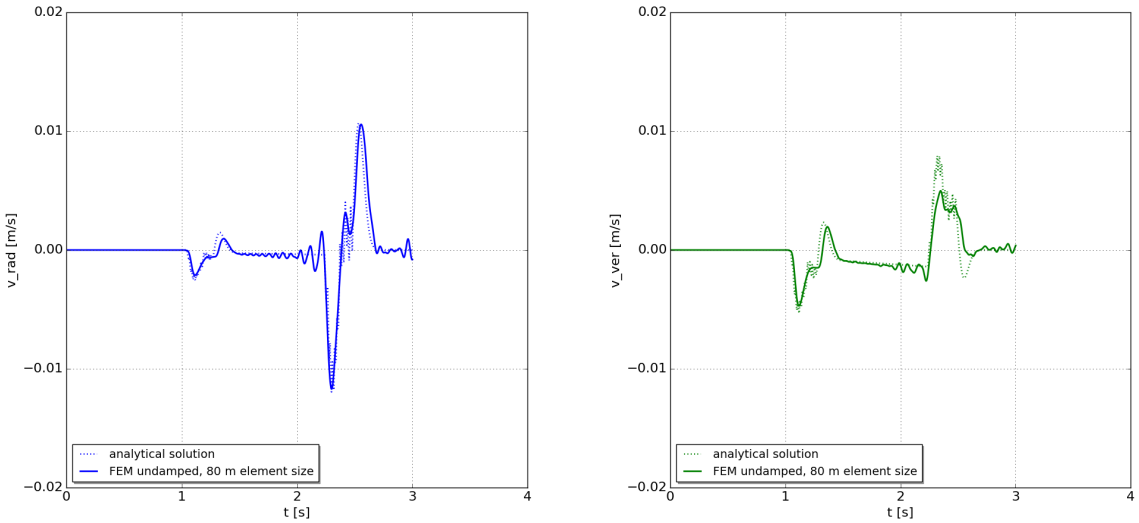

Figure C.12 : Radial displacement velocities (blue lines, left) and vertical displacement velocities (green lines, right) of the Middelstum-1 accelerometer according to the FEM simulation (solid lines) and the analytical solution (dotted lines). The source and conditions are described in the text.
The seismic source in the analytical calculation is represented by a series of 21 moment tensors along fault strike. The source time function for the generated wave approximates is the modified source time function Eq. (3.1.5) with shape parameters t_r = 0.08 s, n = 2. The rupture starts at the centre of the source on the z-axis and propagates with a rupture velocity V_r = 2 km/s in north and south directions along fault strike.
The comparison is satisfactory for the purpose of this work. Note that there is a small time difference between the arrival times of the waves for both solutions. Further, the FEM simulation does not capture the last peak in the vertical velocity and generates small oscillations with a frequency of about 10 Hz which correspond with the fringes upfront of the shear wave shown in Figure C.11 .

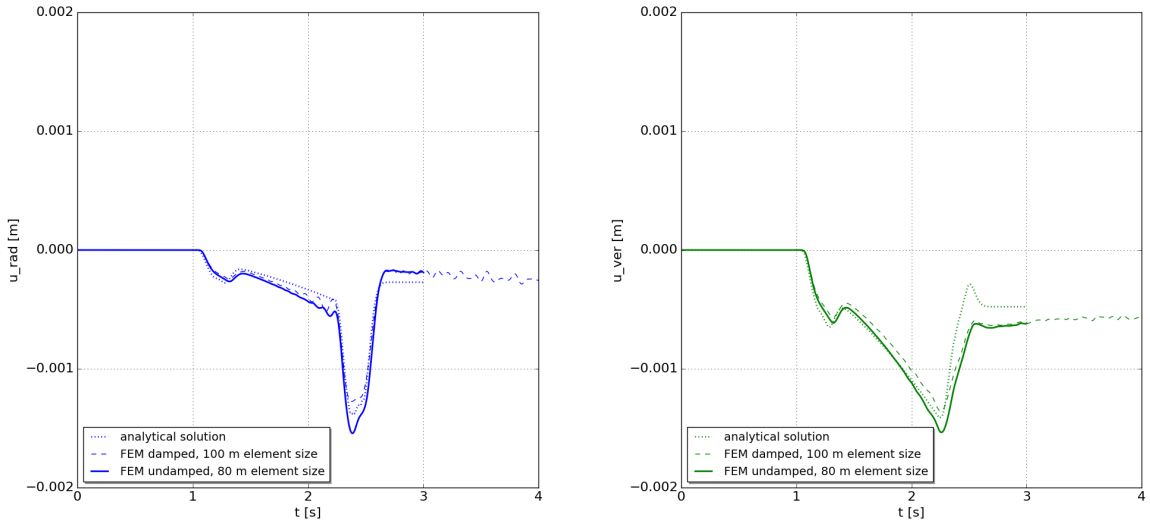

Figure C.13 : Radial displacements (blue lines, left) and vertical displacements (green lines, right) of the Middelstum-1 accelerometer according to the FEM simulation (solid and dashed lines) and the analytical solution (dotted lines). The domain, source and conditions are described in the text.
The solid lines are for a simulation with a maximum element size of 80 m. The dashed lines are for a simulation with a maximum element size of 100 m which also includes wave damping.

Appendix D

Relation between seismic moment, size of rupture plane and corner frequency

Appendix D.1 Seismic moment and size of rupture plane

The seismic moment of a tremor M_0 [Nm] is given by

$$M_0 = \mu S D. \tag{D.1.1}$$

μ [Pa] is the shear modulus of the rock, S the surface of the slip plane and D [m] is the mean relative slip displacement, i.e. the mean slip between the two sides of the slip plane. For a circular slip plane, the seismic moment relates to the stress reduction $\Delta\tau$ [Pa] over this plane due to slippage as, see for example Scholz (2002), Eq. 4.30,

$$M_0 = \frac{16}{7}\Delta\tau R^3. \tag{D.1.2}$$

R [m] is the radius of a circular slip plane. Vice versa,

$$R \sim \left(\frac{7}{16}\frac{M_0}{\Delta\tau}\right)^{1/3}. \tag{D.1.3}$$

For a rectangular slip plane with length L [m] and width W [m] and where the slip is parallel to L, according to Stein and Wysession (2003), §4.6.3, Eq. 20,

$$L \sim \left(\frac{8}{3\pi c_{WL}}\frac{M_0}{\Delta\tau}\right)^{1/3} \quad \text{or} \quad L \sim \left(\frac{8}{3\pi W}\frac{M_0}{\Delta\tau}\right)^{1/2}. \tag{D.1.4}$$

$c_{WL} = W/L$ [-]. For a square slip plane $c_{WL} = 1$. For the same seismic moment M_0, the length of a square plane L is about 0.7 times smaller than the diameter of the circular

plane $2R$.

According to Leonard (2010), it is generally accepted that the seismic moment M_0 of natural earthquakes scales with the slip area S [m^2] as $M_0 \propto S^{3/2}$. This holds even for considerable aspect ratio's L/W. According to Eq. (D.1.1), this implies that the slip length scales as $D \propto S^{1/2}$.
Combining Eqs. (D.1.1) and (D.1.4) where $S = WL$ [m^2] is the surface area of the slip plane,

$$D = \frac{3\pi}{8}\frac{\Delta\tau}{\mu}L. \tag{D.1.5}$$

For small tremors and for constant S, $D \propto L$, in accordance with Leonard (2010). One may ask whether this also holds for long rupture planes along fault strike which remain confined in the reservoir and with slip direction primarily along fault dip. In the case that the slip displacement is bounded by the reservoir thickness but occurs over a distance along fault strike of many times the reservoir thickness, the seismic energy would be proportional to the length of the slip plane L along fault strike and herewith $M_0 \propto S$.

The seismic moment for the largest circular or largest square slip plane, which resides in a fault plane with throw t_{res} in a reservoir with reservoir height h_{res}, follows from these expressions by inserting $R = W_{res}/2$ or $L = W_{res}$ and $c_{WL} = 1$ where $W_{res} = h_{res} + t_{res}$ into Eqs. (D.1.2) and (D.1.4), i.e.

$$M_0 \sim \frac{2}{7}\Delta\tau W_{res}^3 \quad \text{and} \quad M_0 \sim \frac{3\pi}{8}\Delta\tau W_{res}^3. \tag{D.1.6}$$

The pre-factors differ somewhat. Vice-versa,

$$W_{res} \sim c\left(\frac{M_0}{\Delta\tau}\right)^{1/3} \quad \text{where} \quad c \sim 0.6 - 1. \tag{D.1.7}$$

For $\Delta\tau = 1$ MPa, $W_{res} = 300$ m and $\mu = 6.2$ GPa, we obtain from these expressions $M_0 = 8$ TJ or $M_0 = 32$ TJ or seismic magnitudes $M = 2.5$ and $M = 2.9$, respectively[1].

Table D.1 shows the rupture plane length L for a ribbon-like rupture plane for various seismic magnitudes. For a magnitude $M > 4.5$, the slip plane would obtain the shape

[1]We use the relation between seismic moment and seismic magnitude from Hanks and Kanamori (1979), i.e. $M = 2/3 \log M_0 - 6.1$.
A shear modulus $\mu = 6.2$ GPa refers to the mechanical strength properties of the Groningen reservoir rock (assuming a typical Young modulus $E = 15$ GPa and a Poisson ratio $\nu = 0.2$). This value is lower than the shear modulus derived from for the shear wave velocity in the reservoir. The latter is equal to $\mu = \rho V_s^2$. Using $V_s = 2.2$ km/s and $\rho = 2200$ kg/m^3, we obtain $\mu \sim 10$ GPa.
The combination $\Delta\tau = 1$ MPa, $\mu = 6.2$ GPa gives a ratio $\Delta\tau/\mu \sim 1.6\ 10^{-4}$. The combination $\Delta\tau = 1.6$ MPa, $\mu = 10$ GPa would give the same ratio. The latter value of $\Delta\tau$ is in the range of expected values for the Groningen field according to Kraaijpoel and Dost (2013).
In general, higher break-down stresses lead to smaller rupture planes for the same seismic magnitude.

of a very long ribbon if $L \propto M_0^{1/2}$. Also, the value for the slip distance D, obtained from Eq. (D.1.5), would become unrealistically large for this rupture plane. If $L \propto M_0$, a similar long ribbon-like rupture plane would be obtained for $M > 4$.
On the other hand, if the slip plane of a tremor with magnitude $M = 4$ would penetrate into the carboniferous underburden and remains equi-dimensional, $L \propto M_0^{1/3}$. If the slip plane would be circular, the radius $R \sim 0.85$ km according to Eq. (D.1.3) and for $\Delta\tau =$ 1 MPa and $\mu = 6.2$ GPa.

Table D.1 : Rupture plane length L and slip distance D for ribbon-like rupture planes for various moment magnitudes M according to Eqs. (D.1.4) and (D.1.5).
The width of the rupture plane $W = 300$ m. The shear modulus of the reservoir rock used is $\mu = 6.2$ GPa. The stress drop is $\Delta\tau = 1$ MPa. For a constant seismic moment M_0 and rupture plane width W, $L \propto (\Delta\tau)^{-1/2}$ and $D \propto (\Delta\tau)^{1/2}$.

mom. magnitude	seismic moment	width	length	slip
M	M_0	W	L	D
Richter	PJ	km	km	m
.....	.....	.....	.....	.....
3.6	0.3	0.3	0.9	0.17
4	1.4	0.3	2.0	0.38
4.5	7.9	0.3	4.7	0.90

Appendix D.2 Corner frequency

Far-field ground motions from a reasonable kinematic model of a tremor is expected to have a spectrum with a constant value at low frequencies and proportional to a negative power of frequency at high frequencies. Following Aki and Richards (2009), the corner frequency is defined as the frequency at the intersection of the low- and high-frequency asymptotes in the spectrum. In signals as a function of time, the period of the lowest dominant oscillation is a good indication of the corner frequency.

In general, the corner frequencies of P and S waves can differ, see e.g. Aki and Richards (2009), §10.1.7. This is observed and modelled. A rough estimate of the corner frequency f_c [Hz] of a rupture in a circular plane the seismic spectrum follows from, see Scholz (2002), §4.3.2,

$$f_c \sim \frac{1}{t_R} \sim C\frac{V_r}{R}, \tag{D.2.1}$$

where t_R [s] is the duration of the rupture, V_r [m/s] is the rupture velocity, R [m] is the radius of the slip plane and C [-] is a constant of order 1. A useful estimate for V_r is $V_r \sim 0.8V_s$ where V_s [m/s] is the shear velocity in the rock surrounding the rupture plane. Vice-versa, the radius of the rupture plane can be derived from

$$R \sim C' \frac{V_s}{f_c}. \tag{D.2.2}$$

For the S wave, $C' \sim 0.37$, according to Udias et al. (2014), Eq. 9.27[2]. So, a large tremor with a corner frequency of $f_c = 2$ Hz and a shear velocity $V_s = 2.2$ km/s, could originate from a circular rupture plane with a radius $R \sim 0.3$ km.

For a rectangular fault of length L and width W, according to Udias et al. (2014), Eqs. 8.5 and 8.6,

$$\sqrt{LW} \sim \frac{1.7}{2\pi} \frac{V_p}{f_c^p} \quad \text{and} \quad \sqrt{LW} \sim \frac{3.8}{2\pi} \frac{V_s}{f_c^s}. \tag{D.2.3}$$

For the S wave, the equivalent radius of this plane would be $R_{eq} = 1/\sqrt{\pi LW} \sim 0.34V_s/f_c^s$.

So, a reasonable estimate for the equivalent radius of the rupture plane would be $R \sim 0.3V_s/f_c^s$ where V_s is the shear wave velocity in the rock around the rupture plane and f_c^s is the corner-frequency of the shear wave.

[2]Using the radial or angular corner frequency $\omega_c = 2\pi f_c$, the authors use $R = 2.34V_s/\omega_c$. This value is somewhat higher than the value $C' \sim 0.28$ derived by Sato and Hirasawa for a circular slip plane, see Aki and Richards (2009), §10.1.7, Eq. 10.35.